# Detecting vulnerability of humid tropical forests to multiple stressors

Sassan Saatchi, Marcos Longo, Liang Xu, Yan Yang, Hitofumi Abe, Michel André, Juliann Aukema, Nuno Carvalhais, Hinsby Cadillo-Quiroz, Gillian Ann Cerbu, et al.

One Earth

Article

# Detecting vulnerability of humid tropical forests to multiple stressors

## Graphical abstract

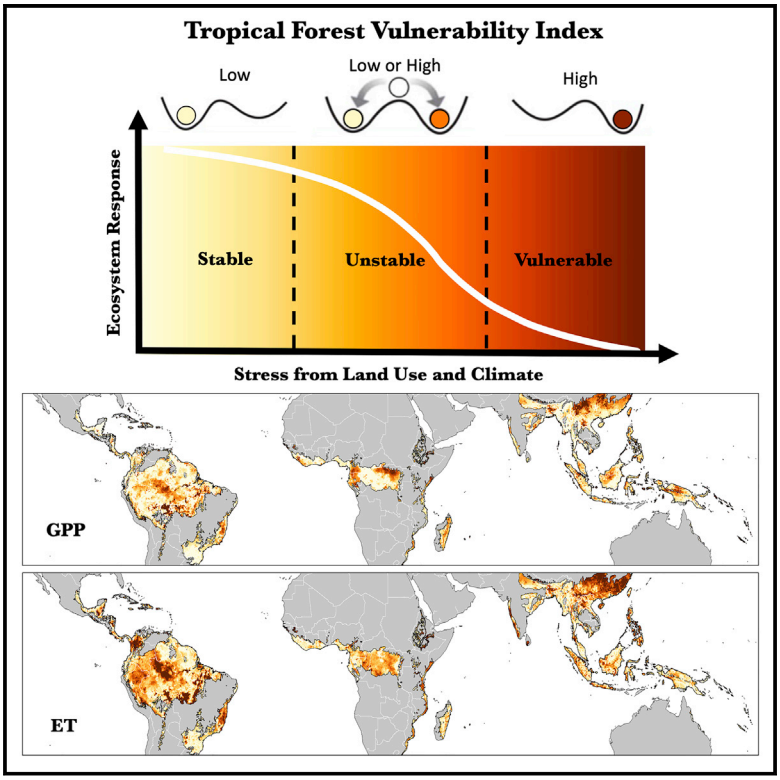


## Highlights

- An index to track vulnerability of global rainforests to climate and land use
- Four decades of satellite data show widespread vulnerability across the tropics
- Response of rainforests to heat and drying varies across the continents
- Early warning from the index can identify regions for conservation and restoration

## Authors

Sassan Saatchi, Marcos Longo, Liang Xu, ..., Sylvia N. Wilson, Steven Brumby, Aurora C. Elmore

## Correspondence

saatchi@jpl.nasa.gov

## In brief

Rainforests take hundreds of years to be formed into a diverse and complex structure that is lush but fragile. The reason for their fragility is the difficulty to recover from disturbance. Using satellite observations, we show how increasing threats from large-scale deforestation and severe climate conditions over the past four decades have substantially impacted the ecological functions of these forests regionally, pushing them toward a critical point of no recovery and a dryer and less diverse state.

Saatchi et al., 2021, One Earth *4*, 988–1003
July 23, 2021 
https://doi.org/10.1016/j.oneear.2021.06.002

CellPress

CellPress
OPEN ACCESS

Gold Standard for the Global Goals
3 tons of $CO_2$ offset

One Earth

Article

# Detecting vulnerability of humid tropical forests to multiple stressors

Sassan Saatchi,[1,2,51,*] Marcos Longo,[1] Liang Xu,[1] Yan Yang,[1] Hitofumi Abe,[3] Michel André,[4] Juliann E. Aukema,[5] Nuno Carvalhais,[6,7] Hinsby Cadillo-Quiroz,[8] Gillian Ann Cerbu,[9] Janet M. Chernela,[10] Kristofer Covey,[11] Lina María Sánchez-Clavijo,[12] Isai V. Cubillos,[13] Stuart J. Davies,[14] Veronique De Sy,[15] Francois De Vleeschouwer,[16] Alvaro Duque,[17] Alice Marie Sybille Durieux,[18] Kátia De Avila Fernandes,[19] Luis E. Fernandez,[20] Victoria Gammino,[21] Dennis P. Garrity,[22] David A. Gibbs,[22] Lucy Gibbon,[5] Gae Yansom Gowae,[23] Matthew Hansen,[24] Nancy Lee Harris,[22]

*(Author list continued on next page)*

[1]Jet Propulsion Laboratory, California Institute of Technology, 4800 Oak Grove Drive, Pasadena, CA, USA
[2]Institute of Environment and Sustainability, University of California, Los Angeles, CA, USA
[3]Food and Agricultural Organization of the United Nations, Papua New Guinea
[4]Laboratory of Applied Bioacoustics, Technical University of Catalonia, Barcelona, Spain
[5]United States Agency for International Development, Washington, DC, USA
[6]Max Planck Institute for Biogeochemistry, Jena, Germany
[7]Departamento de Ciências e Engenharia do Ambiente, Universidade Nova de Lisboa, Caparica, Portugal
[8]School of Life Sciences, Arizona State University, Tempe, AZ, USA
[9]World Bank Group, Washington, DC, USA
[10]Department of Anthropology, University of Maryland, College Park, MD, USA

*(Affiliations continued on next page)*

**SCIENCE FOR SOCIETY** Rainforests are being lost at an alarming rate due to deforestation and degradation. As these forests lose their intactness and diversity, their resilience to climate change declines and they become more vulnerable to droughts and wildfires. Here, we built a spatially explicit tropical forest vulnerability index (TFVI) based on observations of forest cover, carbon, and water fluxes to identify areas where rainforests are losing resilience to disturbance and are changing toward an irreversible state, a "tipping point." Our findings show how and where tipping points may occur, either as a gradual downhill decline of ecosystem services or an abrupt change. We present TFVI as an index to monitor tropical forests and provide early-warning signals for regions that are in need of policies that simultaneously promote conservation and restoration to increase resilience and climate mitigation.

## SUMMARY

Humid tropical forests play a dominant role in the functioning of Earth but are under increasing threat from changes in land use and climate. How forest vulnerability varies across space and time and what level of stress forests can tolerate before facing a tipping point are poorly understood. Here, we develop a tropical forest vulnerability index (TFVI) to detect and evaluate the vulnerability of global tropical forests to threats across space and time. We show that climate change together with land-use change have slowed the recovery rate of forest carbon cycling. Temporal autocorrelation, as an indicator of this slow recovery, increases substantially for above-ground biomass, gross primary production, and evapotranspiration when climate stress reaches a critical level. Forests in the Americas exhibit extensive vulnerability to these stressors, while in Africa, forests show relative resilience to climate, and in Asia reveal more vulnerability to land use and fragmentation. TFVI can systematically track the response of tropical forests to multiple stressors and provide early-warning signals for regions undergoing critical transitions.

 

CellPress
OPEN ACCESS

Sean P. Healey,[25] Robert G. Hilton,[26] Christine May Johnson,[5] Richard Sufo Kankeu,[27] Nadine Therese Laporte-Goetz,[28] Hyongki Lee,[29] Thomas Lovejoy,[30] Margaret Lowman,[31] Raymond Lumbuenamo,[9] Yadvinder Malhi,[32] Jean-Michel M. Albert Martinez,[33] Carlos Nobre,[34] Adam Pellegrini,[35] Jeremy Radachowsky,[36] Francisco Román,[37] Diane Russell,[38] Douglas Sheil,[39] Thomas B. Smith,[40] Robert G.M. Spencer,[41] Fred Stolle,[22] Hesti Lestari Tata,[42] Dennis del Castillo Torres,[43] Raphael Muamba Tshimanga,[44] Rodrigo Vargas,[45] Michelle Venter,[46] Joshua West,[47] Atiek Widayati,[48] Sylvia N. Wilson,[49] Steven Brumby,[50] and Aurora C. Elmore[50]

[11]Environmental Studies and Sciences Program, Skidmore College, Saratoga Springs, NY, USA
[12]Instituto de Investigación de Recursos Biológicos Alexander von Humboldt, Bogotá, Colombia
[13]The Nature Conservancy, Bogota, Colombia
[14]Forest Global Earth Observatory, Smithsonian Tropical Research Institute, Washington, DC, USA
[15]Laboratory of Geo-Information Science and Remote Sensing, Wageningen University Droevendaalsesteeg 3, 6708 PB Wageningen, the Netherlands
[16]Instituto Franco-Argentino para el Estudio del Clima y sus Impactos (UMI 3351 IFAECI/CNRS-CONICET-UBA-IRD), Ciudad Autonoma de Buenos Aires, Argentina
[17]Departamento de Ciencias Forestales, Universidad Nacional de Colombia, Medellín, Colombia
[18]Descartes Labs, Santa Fe, NM, USA
[19]Department of Geoscience, University of Arkansas, Fayetteville, AR, USA
[20]Department of Biology, Wake Forest University, Winston-Salem, NC, USA
[21]Dornsife School of Public Health, Drexel University, Philadelphia, PA, USA
[22]World Resources Institute, Washington, DC, USA
[23]Department of Environmental Science and Geography, University of Papua New Guinea, Port Moresby, Papua New Guinea
[24]Department of Geographical Sciences, University of Maryland, College Park, MD, USA
[25]U.S. Forest Service, Rocky Mountain Research Station, Ogden, UT, USA
[26]Department of Geography, Durham University, Durham, UK
[27]Department of Geography, ESO Lab., Université du Maine, Le Mans, France
[28]School of Forestry, Northern Arizona University, Flagstaff, AZ, USA
[29]Department of Civil and Environmental Engineering, University of Houston, Houston, TX, USA
[30]George Mason University, Fairfax, VA, USA
[31]TREE Foundation, Sarasota, FL, USA
[32]Environmental Change Institute, School of Geography and the Environment, University of Oxford, Oxford OX1 3QT, UK
[33]Géosciences Environnement Toulouse (GET), IRD/CNRS, Université Toulouse (UPS), Toulouse, France
[34]Institute for Advanced Studies, Universidade de São Paulo, São Paulo, SP CEP 05508-060, Brazil
[35]Department of Plant Sciences, University of Cambridge, Cambridge, UK
[36]Wildlife Conservation Society, Washington, DC, USA
[37]Center for Amazonian Scientific Innovation, Wake Forest University, Madre de Dios, Peru
[38]SocioEcological Strategies, Inc., Washington, DC, USA
[39]Norwegian University of Life Sciences, Southern Cross University, As, Norway
[40]Institute of the Environment and Sustainability and Department of Ecology and Evolution University of California, Los Angeles, CA, USA
[41]Department of Earth, Ocean, and Atmospheric Science, Florida State University, Tallahassee, FL, USA
[42]Forest Research and Development Centre, Bogor, Indonesia
[43]Instituto de Investigaciones de la Amazonia Peruana, Iquitos, Peru
[44]Congo Basin Water Resources Research Center, University of Kinshasa, Kinshasa, Democratic Republic of Congo
[45]Department of Plant and Soil Sciences, University of Delaware, Newark, DE, USA
[46]Ecosystem Science Management Program, University of Northern British Columbia, Prince George, BC, Canada
[47]Department of Earth Sciences, University of Southern California, Los Angeles, CA 90089, USA
[48]Tropenbos Indonesia, Bogor, Indonesia
[49]United States Geological Survey, Reston, VA, USA
[50]National Geographic Society, Washington, DC, USA
[51]Lead contact
*Correspondence: saatchi@jpl.nasa.gov
https://doi.org/10.1016/j.oneear.2021.06.002

## INTRODUCTION

Humid tropical forests (HTFs) (Figure S1) are hyper-diverse and play a dominant role in the functioning of Earth and regulating its climate by accounting for more than half of its life forms, one-third of its metabolic activity, and storing more than half of its vegetation carbon.[1,2] These forests benefit from relatively warm temperature and high rainfall in equatorial regions that support the storage and processing of larger amounts of carbon via plant productivity and ecosystem respiration than any other biome.[3] During the dry season, tropical trees are the primary source of water released to the atmosphere through evapotranspiration (ET), creating rainfall locally and thousand miles away to maintain their moist environment.[4] These processes have been maintained regularly for millennia with intact forest structure and diversity and stable ecological functions.[2]

However, HTFs are under increasing threats from human-induced and environmental stressors.[5–7] Between 15% and 20% of HTFs have been cleared since the early 1990s and at least an additional 10% have been degraded.[8] Widespread

decline of carbon storage and productivity has been reported regionally due to elevated temperature and droughts.[9–11] Water and energy exchanges are suppressed significantly from forest degradation or drying atmosphere.[12] Remaining forests are changing into increasingly smaller fragments with substantial biodiversity loss.[13] With the projected rate of climate change and escalating land-use activities, these forests will lose their current capacity for global carbon sink and may even become a source of carbon to the atmosphere via changing photosynthesis and respiration rates, losing biodiversity, increasing tree mortality from droughts, and widespread forest collapse via fire.[14]

Over recent decades, HTFs have grown increasingly vulnerable to these pressures with high probability of undergoing regime shifts.[15] Climate models predict either a tipping point of tropical forests in the form of large-scale tree mortality[16] or a more gradual continuous transition to a drier and fire-dominated savanna-like ecosystem,[17] both with large uncertainties in future trajectories.[18] There is ample evidence from local studies and ecosystem modeling that the HTF vulnerability is eminent,[18–20] but how forest vulnerability varies across space and time and what level of stress forests can tolerate before facing a tipping point are poorly understood.[21] This raises the question of whether one can detect the vulnerability of tropical forests to human- and climate-induced stressors spatially and identify areas of low resilience that may drive the ecosystem to an alternative state.

Here, we address this challenge in two ways. First, we used time series of climate data, satellite records, and models to track stressors and ecosystem responses over four decades (1982–2018). We define a stressor as a condition, event, or a trend related to climate variability and change or forest disturbance that can exacerbate hazards on ecosystems. This provides the first pan-tropical test (Figure S1) of the degree to which the putative predictors of HTF changes (e.g., vapor pressure deficit, water balance, and forest cover) vary spatially and remain consistent over time in magnitude and trends. All spatial data were gridded at $0.1^{\circ} \times 0.1^{\circ}$ (120 $km^2$) resolution (experimental procedures). For climate stress, the predictors include trends in temperature (T), vapor pressure deficit (VPD), and water balance (WB) and for human-induced stress, we used forest tree cover (TC) changes from deforestation, degradation, and fire. For ecosystem responses, we focused on the carbon cycle and included the above-ground live biomass (AGB) (2000–2018),[22] gross primary production (GPP) (1982–2018), ET (1982–2018), and the vegetation skin temperature (land surface temperature [LST]) (2000–2018) as variables linking the water and energy balance processes with the forest carbon cycling.[23]

Second, we used AR1 autoregressive models to quantify the temporal autocorrelation and the sensitivity of the ecosystem carbon cycle responses to multiple stressors. We included climate variables (WB, VPD) and TC changes in AR1 model with 1-month-lagged GPP, ET, and LST or 1-year-lagged AGB response variables to identify regions exhibiting amplified responses to land-use and climate variability and trends (experimental procedures). We define vulnerability as the degree to which a system is susceptible to, or unable to cope with, adverse effects of disturbance, such as the stress from climate change, including climate variability and extremes.[24] Vulnerability can be considered as an estimate of the inability of the ecosystem to tolerate stressors.[25] This occurs when the ecosystem starts modulating its responses to stressors over time and space and starts losing its resilience or the ability to recover from disturbance.[26] To quantify resilience, we evaluated the temporal autocorrelation between each response and stress variables on the monthly time scales after removing the seasonal cycles and trends. Higher temporal autocorrelation points to the slow recovery of the ecosystem if it is exposed to severe stress, which can be considered an important early-warning indicator of critical transitions.[27,28] We then used additive regression AR1 models to simultaneously assess the relationship of temporal autocorrelation to multiple stressors.[29,30] The coefficients of the 1-month-lagged response variables can be used to identify regions sensitive to stress and/or with the memory effects and to develop a spatially explicit tropical forest vulnerability index (TFVI) that shows changes of the response variables to long-term trends of multiple stressors. The magnitude and spatial variations of TFVI can identify areas across the tropics that exhibit high vulnerability and risks of a critical transition.

## RESULTS

### Patterns of forest stressors

We quantify land-cover and land-use change (LCLUC) stress across the tropics using the spatial variations of TC change and burned area from fire from 1982 to 2018 (Figures 1A and 1B). The percent of TC change at the grid cells includes loss of forest from deforestation and degradation and gain from secondary forest recovery, and afforestation relative to the benchmark forest cover of 1982 (experimental procedures). Changes of TC show that, in the 1980s, more than 340 Mha ($10^6$ hectares) of tropical forests experienced a net loss (gain-loss) of tree cover, which became more widespread in the 1990s (~390 Mha) and 2000s (~420 Mha), but dropped significantly in 2010s to about 300 Mha (Figure S2). TC loss exhibited uneven patterns globally and across time, with large-scale deforestation and agricultural expansion in the Americas, to small-scale shifting cultivation in Central Africa, and a combination of agroforestry and commodity-driven agriculture in Asia.[31] The net loss of TC was consistently higher in the Americas, with an average rate of 2.5 Mha $year^{-1}$ in the 1980s, 1.2 Mha $year^{-1}$ in the 1990s, 2.0 Mha $year^{-1}$ in the 2000s, and 1.6 Mha $year^{-1}$ in the 2010s. In Africa, the highest rate of TC loss was about 0.6 Mha $year^{-1}$ from 1982 to 1999 but it dropped significantly to about 0.15 Mha $year^{-1}$ from 2000 to 2018. More recently (2000–2018), the gross TC loss was about 7.3 Mha $year^{-1}$, which is comparable with 7.65 Mha $year^{-1}$ of average rate of forest clearing extracted from the Landsat-based (30-m resolution) forest cover change products (Figure S3).[32]

Wildfire impacts on forest cover remained confined to areas where deforestation and human activities are concentrated or across forest-savanna boundaries (Figure 1B). We found the annual rate of burned area (BA) in forest pixels across all HTFs is about 21 Mha $year^{-1}$ averaged from 1982 to 2018. This estimate may be larger than real area of fire burns due to the coarse resolution of satellite data (500 m) and partial burns within each pixel. Time series of percent of BA show that fire disturbances in the African tropical forests are twice more prevalent and have

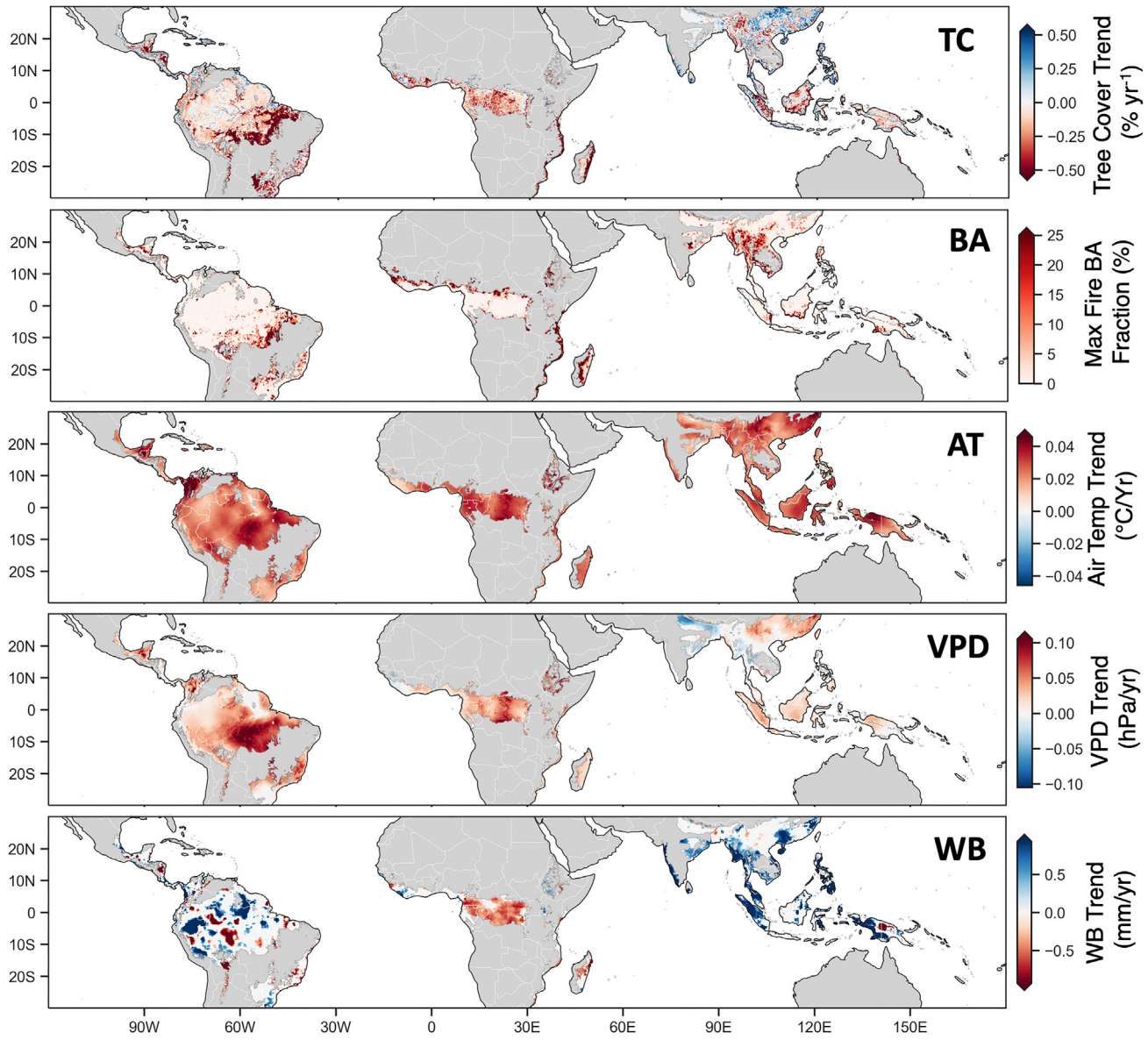


**Figure 1. Spatial patterns of stressors across humid tropical forests**

Patterns of LCLUC indicators are shown as: the trend of annual TC change (1982–2018) capturing deforestation and degradation, and average of maximum fraction of fire burned area (BA) at the pixel over the entire time series (1982–2018). Patterns of climate stressors are shown using trends of air temperature (AT), VPD, and WB from 1982 to 2018 (see experimental procedures).

larger interannual variability than fires in other continents (Figure S4). Our results suggest that forest fire and other land-use change activities impact approximately 10–15 Mha year$^{-1}$ (not accounting the overlapped areas) (experimental procedures), causing the reduced intact forests area (>50% TC) from 1,300 Mha in 1982 to less than 1,000 Mha at the end of 2018.

Increasing climate variability and change further exacerbates the land-use stress on tropical forests. Trends of air temperature (Figure 1C) show that regions in the southeast and northwest of the Amazon, Central and West Africa, and tropical Asia have experienced an increase of more than 0.4°C per decade. While tropical forests may show strong resilience to increased temperature,[33] the warming trend is also accompanied by atmospheric drying represented by VPD. We find an extensive increase of VPD (>0.01 hPa year$^{-1}$) in South America and Central Africa (Figure 1D), including severe anomalies across regions in the southeastern Amazon and Congo Basins during drought years (Figure S5). The VPD trend shows a potential turning point from the early 2000s with approximately 1.5 times larger increase than the first two decades (1982–1999), suggesting a substantially more stress from atmospheric drying across the tropical forests in the last two decades.[34]

Impacts of droughts and water stress on tropical forests are detected by the spatial variations of the WB as the difference

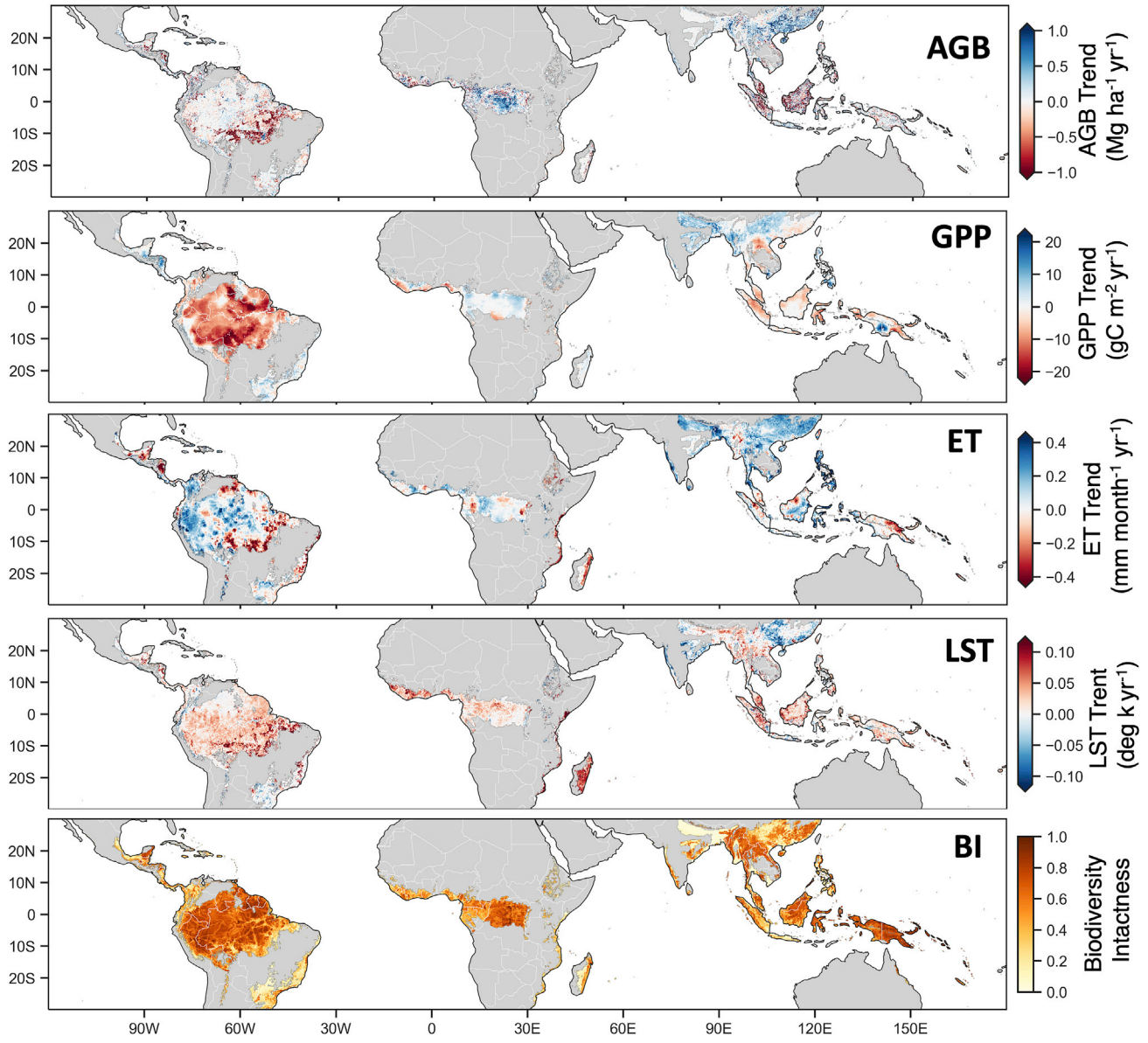


**Figure 2. Spatial patterns of responses across humid tropical forests**

Patterns of ecosystem responses are shown as: the trend of AGB from 2000 to 2018, the trend of GPP from 1982 to 2018), the trend of ET from 1982 to 2018, the trend of the LST from 2000 to 2018, and biodiversity intactness (BI) showing present state biodiversity habitat across the tropics (see experimental procedures).

between monthly water supply from precipitation and the water loss from potential ET (experimental procedures). Trends of WB from 1982 to 2018 (Figure 1E) show heterogeneous and divergent patterns with negative trends developing across the Congo Basin and areas in the south and southwestern Amazon. In contrast, we found increasing water availability in Asia and the northwestern Amazon. However, trends alone may not capture the water stress across the tropics. Stress from WB increases from seasonal anomalies of rainfall and during episodic droughts.[7,35,36] The negative trend of rainfall during the driest quarter shows that the western Amazon and its headwaters are emerging as the largest region of seasonal rainfall decline in recent decades (Figure S6). Rainfall trends are more heterogeneous across African and Asian forests, showing patterns of increasing rainfall (Figure S6).

## Patterns of forest responses

Among ecological responses, we focus on processes associated with the forest carbon cycling by including changes in live AGB from 2000 to 2018, the GPP from 1982 to 2018, ET from 1982 to 2018, and day-time LST from 2000 to 2018, which links forest carbon fluxes with energy cycles and is closely related to forest canopy temperature. Trend analysis shows the spatial patterns of these responses across the tropics (experimental procedures) (Figure 2). We found significant biomass loss in the southern and eastern Amazon and along the Andean

foothills, Central America, West Africa, and Insular Asia (Figure 2A), where deforestation and degradation have been persistent and widespread (Figure S3). Trends of live biomass across tropics also show extensive areas of forest biomass gain, most importantly in the central and northern Congo Basin and mainland Asia and southern China. Increasing biomass in the Congo Basin may be attributed to the decline of the LCLUC stress[6] and stable productivity due to climate conditions and atmospheric $CO_2$ fertilization.[37] Increases in biomass in southern China are associated with recent intensive forestry, which significantly expanded across the region over the last 20 years.[38]

Forest productivity shows widespread and strong negative trends in the Amazon Basin over the entire time series (Figure 2B) influenced by frequent droughts, increasing temperature, and VPD since the early 2000s (see supplemental information) (Figure S5). In contrast, forests of the Congo Basin show stable and even increasing carbon productivity in northern and eastern regions (Figure 2B). Forest productivity shows positive trends in large areas of mainland Asia, southern China, and Central America, mostly due to widespread forest recovery from past disturbance, afforestation in recent years, and climate conditions favorable to GPP increase, such as increasing radiation and rainfall.[38,39]

ET shows a declining trend (Figure 2C), mostly in areas impacted by the LCLUC across the tropics. Southern Amazon, with large-scale forest conversions since the early 1980s, areas in Central America, West Africa and Madagascar, and Insular Asia, with significant loss of intact forests appear as hotspots of long-term loss of ET. In contrast, large areas across the tropics show increasing trends of ET due to increasing rainfall from the intensification of the hydrological cycle[40] (Figure S5) or forest cover gain (e.g., mainland Asia and southern China) from afforestation and plantation systems.

We used the current state of HTF biodiversity intactness (BI) varying between 0 and 1 and representing the present state of biological and structural integrity of tropical forests (Figure 2E) (experimental procedures). This index is used in our analysis to examine the link between forest resilience and its BI. We found high values of intactness (>0.7) ubiquitous across the central Amazon, Congo Basin, and Asia. However, there are also large areas with lower scores of (<0.4) in the southern and western Amazon, along the foothills of the Andes, and the coastlines where most forest clearing and degradation are concentrated. Wetlands of the Congo Basin exhibit fragmentation from dense hydrographic networks and extensive small-scale agriculture and settlements along rivers (Figure 1A), but remain relatively intact in biodiversity (>0.7). A clear contrast between TC change and BI exists in the mainland and Insular Asia where the landscape is highly fragmented due to forest cover change but the biodiversity remains relatively high (>0.7).

## Continental comparison of stress and response variables

To facilitate a direct comparison of the ecosystem stressors and responses across space and time, we normalized the distribution of each variable to their long-term mean across HTFs using quantile transform and preserved both negative and positive trends (experimental procedures) (Figures 3A and 3B). We represented the cumulative distributions of normalized stress and response variables for each tropical region separately in cart wheel plots (Figures 3C and 3D). Climate and forest disturbance stressors emerge with similar scores but show larger variability across the tropics (Figure C), while ecosystem responses show relatively higher impacts on functions than states and remain less variable across the tropical regions (Figure 3B). HTFs in the Americas experience relatively similar cumulative climate and LCLUC stress with the exception of fire, whereas forests in Africa and Asia are exposed to relatively higher and lower climate and LCLUC stress, respectively. Overall, we find climate stress in each tropical region rivals LCLUC stress to near 0.4–0.6 of the HTF extent in Americas, about 0.4 in Asia and Oceania, and 0.6 in Africa. Their spatial patterns, however, suggest that the responses of ecosystem functions represented by $R_F$ (GPP, ET, LST) are mostly ($R_F > 0.6$) influenced by the patterns of climate stress (Figures S7A and S7C), whereas the ecosystem states (AGB, BI) are mostly ($R_S > 0.6$) impacted by the patterns of forest cover change from LCLUC (Figures S7B and S7D).

## Forest vulnerability and resilience

The temporal autocorrelation of ecosystem responses (AR1 model) shows diverse variations along climate and LCLUC gradients across the three continental regions (Figure 4). The increase in temporal autocorrelation means that the state of the ecosystem on subsequent moments in time become more correlated indicating slower recovery rates (slow down) of the system.[29] Temporal autocorrelation of AGB does not show any significant variation along gradients of WB (or precipitation) (Figures S8A–S8C), while GPP exhibits bimodal patterns in the Americas and Asia (Figures 4A and 4C) and increases markedly in regions with lower annual WB in Africa (Figure 4B). In contrast, ET and LST autocorrelation exhibit higher variability along WB gradients across the three continents (Figures 4B and 4C), indicating the potential slowness and even closeness to critical transitions in regions with typically lower WB, more distinctly in Africa (Figures S8H and S8K). The difference between forests of Africa and other continents disappears in patterns of ET and LST autocorrelation with VPD (Figure S9), showing a gradual but significant slow down when VPD increases. Similarly, temporal autocorrelation of ET and LST also tends to increase with TC, suggesting slow down with the loss of TC (Figure S10).

Using the additive AR1 model with multiple stress variables, we map variations of TFVI for each ecosystem response variable across the tropics (Figure 5). The absolute magnitude of TFVI represents the risk of critical transitions that would result in abrupt decreases (negative values) or increases (positive values) of the response variable given long-term trends in the stressors. The larger the absolute value of TFVI, the greater the risk of a critical transition to either higher or lower value of the ecosystem response. All TFVI values for response variables include uncertainties evaluated from the error propagation of AR1 model coefficients and the data layers used for stress and response variables (experimental procedures).

The TFVI for AGB trend shows extensive areas of south and central Amazon Basin (>91 Mha) with significant vulnerability (TFVI < −2) and transition of ecosystem to a low AGB state (Figure 5A). The TFVI captures the spatial patterns of TC loss and shows strong sensitivity to atmospheric drying conditions represented by increasing VPD in the past two decades (Figure S11).

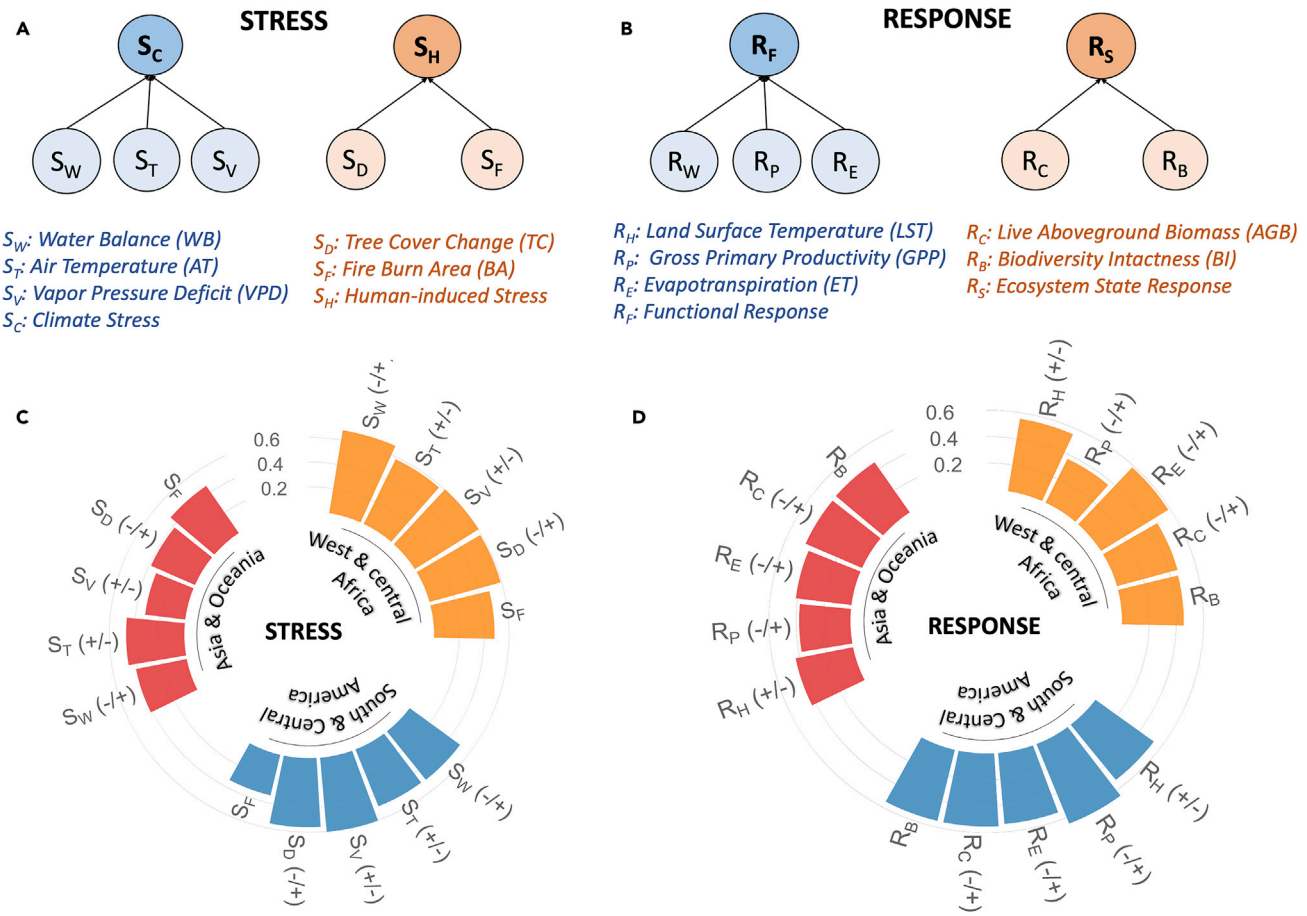


**Figure 3. Relative importance of ecosystem stressors and responses**

Schematic diagram showing at the top panel: (A) indicators of land-use and climate stress and (B) responses of ecosystem function and states. The combined climate-induced ($S_C$) and human-induced stressors ($S_H$) are derived from linear combination of normalized variables (see experimental procedures). The bottom panel shows comparison of stress and responses averaged over regional HTF domains to show their relative importance. The wedges in the wheel charts show the relative significance of (C) ecosystem stressors and (D) responses, with average scores greater than 0.4 for relatively high, 0.2–0.4 for moderate, and less than 0.2 for relatively low strength of stress or impact on the response (see Figure S7).

In contrast, forests in mainland Asia, particularly in the greater Mekong region, show a persistent transition to low AGB state from declining trend of tree cover (sensitivity to TC). African forests, particularly in the Congo Basin, show widespread low sensitivity of AGB to climate. Forest productivity (GPP) on the other hand, exhibits widespread vulnerability in the Amazon Basin (~100 Mha), albeit that most areas show only more moderate risk of sustained reduction (TFVI < −0.5). The notable exceptions are areas under substantial LCLUC stress across the arc of deforestation (Figure 5B) (TVFI < −1). In contrast to these striking patterns across the Amazon, most forests across Africa and Asia show low vulnerability to critical transitions in GPP (Figure 5B) due to the low sensitivity of GPP to climate stress (Figure S12); we even found regions across Africa and Asia that show sustained increase of GPP (Figure 5B) in the east and west of Central Africa due to increasing VPD (potentially more radiation) and mainland Asia and southern China due to increasing forest cover (Figure S12).

The vulnerability of the tropical carbon cycle is also detected in the coupled processes of ET and surface energy balance. The TFVI of ET exhibits two distinct patterns across tropical regions (Figure 5C). Areas with extensive trend in forest cover change in the southern and eastern Amazon (>75 Mha), Central America (>12 Mha), eastern Africa and Madagascar (>40 Mha), and Insular Asia (>9 Mha) show strong risk (TFVI < −1.0) toward a critical reduction of ET. At the same time, extensive regions of tropical forests on all continents exhibit a transition to critically higher ET due to sensitivity to increasing VPD and incoming radiation (Figures S6 and S13). Similarly, LST shows almost ubiquitously high vulnerability of persistent warming across the Americas (>400 Mha) with TFVI > 0.5 (Figure 5D). These areas show increasing LST due to a combination of warming climate, increasing VPD, and large-scale loss of tree cover (>100 Mha) from TC trend. Vulnerability of LST is also due to sensitivity to extreme climate anomalies and water stress during droughts, which impacts heat flux and surface energy balance.[7,41] Contrary to the Americas, LST of forests in Africa shows low sensitivity to climate trends and anomalies except in areas already impacted by widespread LCLUC (eastern Africa and Madagascar). In Asia LST vulnerability is largely due to LCLUC,

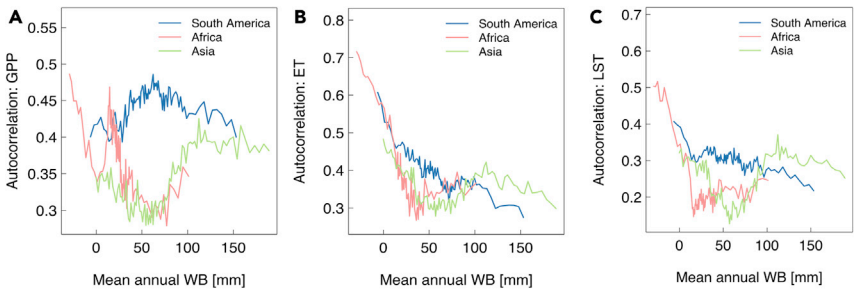


**Figure 4. Slow down of tropical forest ecosystem functions with changes of water balance**

Autocorrelation of GPP (A), ET (B), and LST (C) along the gradient of water stress across different continents. As water balance declines, water stress increases, and changes of the autocorrelation toward higher values indicate the lack of elasticity of the ecosystem to water stress. Higher autocorrelation suggests that the ecosystem is potentially more likely to gradually or abruptly cross the stability threshold and transition to a new state.

with substantial sensitivity to VPD, particularly in mainland Asia and southern China. The uncertainty ranges of TFVI predicted from the error propagation model (Figure S15) have been taken into account to present only regional patterns of vulnerability that are robust.

## DISCUSSION

There are some consistent results emerging from our study: (1) among tropical forests, the Amazon shows significantly more vulnerability to climate and land-use stressors than forests in Africa and Asia, (2) forests in continental Africa, although impacted by similar levels of climate stress as the Amazon, show more resilience, and, in Asia, land-use change drives the forest vulnerability, (3) HTF carbon cycling responses (AGB and GPP) are impacted by climate, but so far show more vulnerability to LCLUC pressures, while ET and LST already show significant transitions attributable to both climate and LCLUC, and (4) the autocorrelation results suggest that, except for areas of large-scale LCLUC, transitions of forests to a critical state appear to be more gradual than abrupt (Figures 4 and S8–S10). These observations and empirically determined patterns agree with results of multiple studies in recent years focused on HTF resilience in local field experiments,[42–44] ecosystem modeling,[16,18,45] and remote-sensing observations.[29,46,47] Our novel approach, however, adds to the increasing evidence by providing patterns of HTF vulnerability based on longer time series of observations (37 years) compared with most observation-based studies. In addition, it allows assessing and quantifying the forest vulnerability based on ecologically important response variables that represent ecosystem states and functions (e.g., AGB, GPP, ET), instead of remote-sensing signals (e.g., optical normalized difference vegetation index)[29] that are indirectly related to the forest function. Finally, our approach produces a spatially explicit index that allows tracking the vulnerability of ecosystem functions to multiple stressors in future.

Differences in patterns of vulnerability at the continental scales are influenced by interactions of recent climate and land-use changes and may also depend on historical human and environmental disturbances, and regional biogeographical and climate variations.[48,49] We examine these interactions in two regions in the Amazon and Congo Basins (boxes in Figure 5). In the Amazon Basin, the regions with highest vulnerability index in GPP and AGB overlap with areas of large-scale forest degradation and fragmentation and significant VPD trend (Figures 1A and 1D). Both AGB and GPP show high sensitivity to these stressors (Figures S11 and S12). In the Congo Basin, on the other hand, the observed vulnerability pattern is the result of complex processes where carbon loss from small-scale degradation caused by shifting cultivation and logging (Figure 1A) interact with the gain from positive trend of AGB from forest recovery (Figure 2A), and moderate rise of VPD (Figure 1D), accompanied by substantial increase in incoming radiation (Figure S6). Such interactions result in overall low sensitivity of AGB and GPP to both climate and TC change, despite some areas showing relatively low resilience in the case of GPP (Figures S11 and S12). The interactions among multiple stressors may also be modulated with a long history of water stress in Africa, making the forests more adapted to droughts. Alternatively, other differences, such as stable available nutrients,[50,51] continental scale biogeography,[52] and contemporary drought tolerant species pools,[53,54] may contribute to continental differences. However, these processes may temporarily reduce the vulnerability of the forest carbon cycling to climate stressors, but these patterns can change drastically as climate forcing increases and larger-scale land-use activities expand across the regions.[55]

Although there is a strong negative trend of WB (increasing water stress) in the Congo Basin compared with the Amazon (Figure 1E), ET and LST show moderate or no trends across the forests. In addition, the patterns of TFVI over the Congo Basin suggest that the LST remains stable and ET shows a potential transition to persistent higher values (Figure 5), mostly driven by a positive sensitivity of ET to increasing VPD (Figure S13) that overcompensates the negative sensitivity to water stress (Figure 1E). We see the increase of temporal autocorrelation with increasing VPD, water stress, and forest cover change in ET and LST in both continents, suggesting a more direct influence of droughts and land-use change on ET and LST.[56] In Asia, there is a moderate increase of LST and ET (Figure 2) but, combined with other climatic and land-use trends in the region, the TFVI shows a relatively high vulnerability with persistent increase in LST in Indonesia, and increased risk of high ET in southern China (Figure 5). These changes can be attributed to the strong sensitivity of LST to atmospheric drying in Java and Borneo (Figure S14), and the tendency of ET to increase as forest cover increases in southern China (Figure S13). Severe precipitation anomaly on forest hydraulic mechanisms can in turn cause increasing tree mortality and declined forest productivity, together resulting in the loss of biomass and GPP, which has been observed in local studies focused on long-term effects of climate.[57–59]

Our results illustrate the conditions under which the ecological functions of tropical forests may slow down or gradually transition to a new state. However, predicting transitions before they

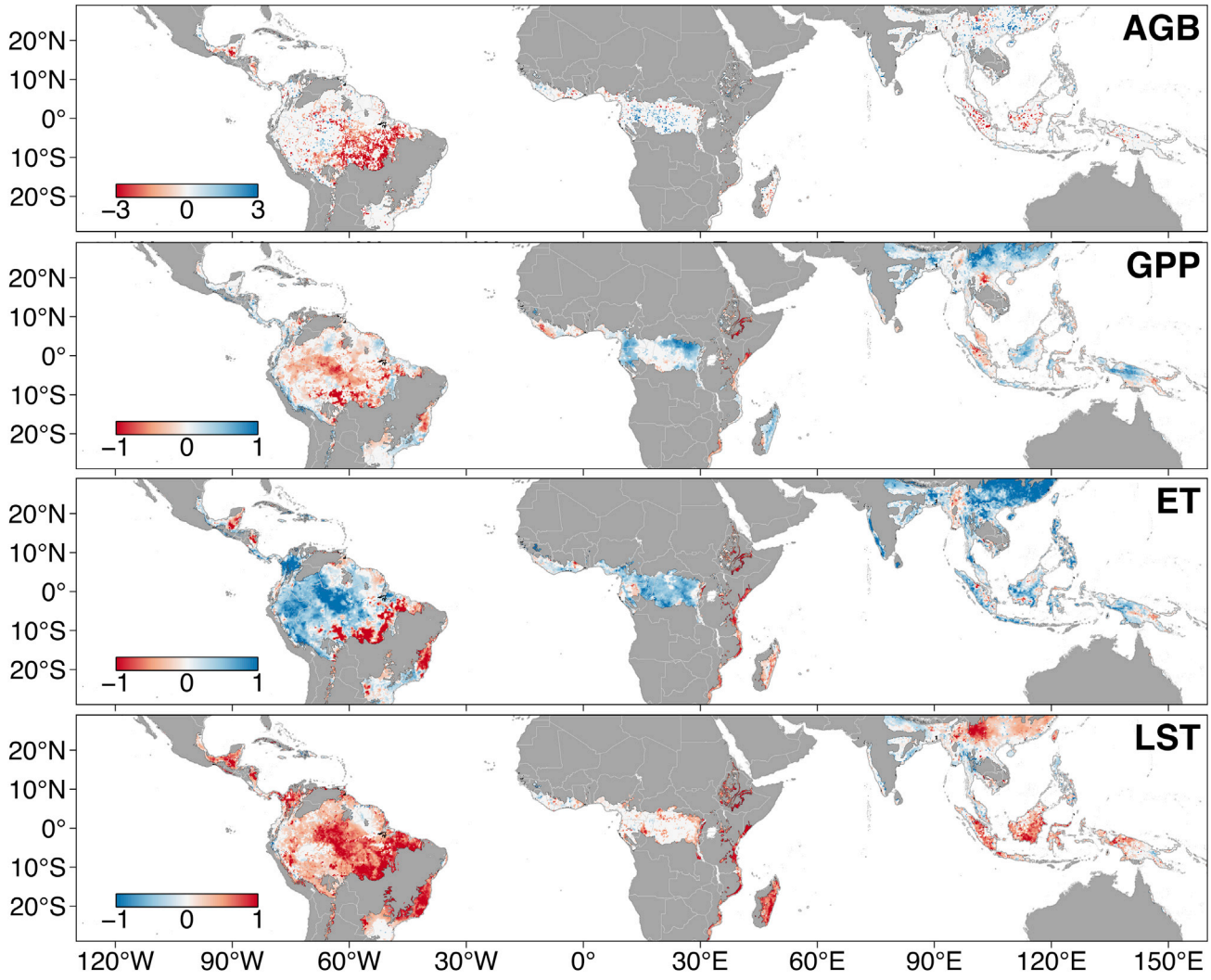


**Figure 5. Humid TFVI**

Maps of vulnerability of humid tropical forests derived from the hybrid autoregression model (hybrid AR1) for above-ground biomass (boxes show areas discussed in the paper), GPP, ET, and LST. The maps shown here are at 0.25° ×0.25° for visualization. Areas with TFVI of approximately zero show stable states and areas with negative (positive) values show stronger risk of sustained slowing down from reduction (increase) of the response variables due to sensitivities to climate or changes of forest cover combined with autocorrelation.

are reached is extremely challenging. The autoregressive model allows us to detect whether the ecosystem is already experiencing vulnerability to climate and LCLUC stressors. This novel approach provides three intrinsic early-warning signals that may indicate if a transition or a tipping point is approaching: (1) sharp rise of autocorrelation indicating how the ecosystem may experience a critical transition if the stress from environmental conditions increases (Figure 4), (2) vulnerability patterns indicating to what extent the sensitivity to climate or LCLUC stress has already pushed the system toward transition (Figure 5), and (3) increased variance of ecosystem response variables (Figures S11–S14). Note that, unlike the striking patterns of the TFVI from the autocorrelation, the increasing variance of the ecosystem response represented by the coefficient of the AR1 model ($\rho \rightarrow 1$)may be less consistent. For AGB, the variance is increasing in areas dominated by the land-use change but has no consistent relationship with respect to climate. In contrast, all other ecosystem responses, GPP, ET, and LST, show relatively consistent increase in variance (using values of $\rho \rightarrow 1$) with respect to climate and land-use changes. The lack of consistency in patterns of variance and TFVI may suggest that the ecosystem vulnerability (e.g., in the case of AGB) may not be robust; however, there are indications that variance is sensitive to other factors that would cause an increase or decline.[29] Examples of this are shown when environmental factors used as stress variables fluctuate stochastically and the ecosystem becomes less sensitive to these factors near the threshold, or when vulnerability or slowing down reduces the ecosystem's capacity to follow high-frequency fluctuations in the stress factors.[27] In our analysis, this inconsistency is more obvious in the case of AGB than other ecosystem responses (GPP, ET, and LST) either because of the effect of shorter time series (2000–2018) or longer

time steps (annual versus monthly) in the analyses. Nonetheless, TFVI is a relatively simple and practical index that contains information about the intensity and direction of vulnerable ecosystem responses, and provides reliable geographical extent and shorter lead times to ecosystem transitions. Whether the early-warning signal can be detected sufficiently early remains unclear.[28]

The consistent vulnerability patterns and the detected temporal autocorrelation for different responses suggest that the slowness of the ecosystem carbon cycling processes is widespread, but with variations in severity across the tropics. Although our results are purely correlational and could conceal competing explanations, the spatial patterns of TFVI appear robust and in agreement with other ground observations. More importantly, our analysis is based on an additive autoregressive model with multiple stressors and it is unlikely that the patterns derived from temporal autocorrelation and TFVI analysis may be artifacts of potential confounding factors.

Satellite observations, even though validated systematically against reference data may have uncertainties in detecting the ecosystem stress and response variables. These uncertainties influence the AR1 model by reducing the autocorrelation and cause either no sensitivity or false resilience to environmental stressors. However, the patterns of vulnerability detected by TFVI remain valid as they depend on higher autocorrelation between stress and response variables that are from independent observations. We performed a detailed uncertainty quantification by propagating errors associated with the remote-sensing observations and the AR1 models for multiple stressors (experimental procedures) and show that the spatial distribution of uncertainty in TFVI for all response variables remain significantly lower than the observed signal in the most vulnerable areas (Figure S15).

The TFVI accounts for multiple factors previously recognized as critical for assessing the vulnerability and sustainability of tropical forests,[24] including the increased exposure to risks (through the long-term trends of stressors, the sensitivity of the ecosystems to stressors), fitted sensitivity parameters, and the resilience of the ecosystem (through the autoregressive coefficient). However, this approach has two important limitations. First, our index does not account for the consequences of vulnerability on societies and socio-ecological systems, including the loss of ecosystem function and states on livelihood dependent on the HTFs—HTF risks, following the IPCC AR5 definition.[60] Second, by using an AR1 model, our approach implicitly assumes stationarity of both the sensitivity and the resilience of the response variables to climate and LCLUC. We opted for a simplified approach with a smaller number of parameters because the time span of the input data available is still relatively short, and with substantial uncertainty (Figure S15). However, the current approach does not account for the changes of the sensitivity and resilience that the system may experience over time. Changes in autoregressive coefficients have been previously proposed as an important metric for the development of early warning for systems approaching tipping points[61] and could be incorporated in the future by expanding the TFVI formulation to be based on autoregressive integrated moving average models with exogenous predictors. Such hybrid models have been used to develop short-term predictions of droughts and fire activity[62,63] and could provide the basis for implementing non-stationary models as longer time series of the main stressors and responses for HTFs become available.

The spatial nature of our approach is based on harnessing a wide range of observations sensitive to ecosystem structure traits and functions. We expect that, with longer records and more advanced satellite observations in the near future, TFVI's ability to provide early-warning signals will significantly improve. Spatial patterns of TFVI can also be used to develop hypotheses and science questions that can be further explored by field experiments and long-term studies. For example, the detection of regions experiencing similar stress but different responses is an ideal case of using TFVI to perform perturbation experiments and examine if the slowness of the ecosystem responses is indeed a reasonable indicator of the ecosystems undergoing critical transitions, such as changes in composition, biodiversity, or carbon cycling.

## EXPERIMENTAL PROCEDURES

### Resource availability

#### *Lead contact*

Further information and requests for resources should be directed to and will be fulfilled by the lead contact, Sassan Saatchi (saatchi@jpl.nasa.gov).

#### *Material availability*

This study did not generate new unique materials.

#### *Data and code availability*

All original satellite and climate data used in the study can be downloaded freely from the following sites: All Moderate Resolution Imaging Spectroradiometer (MODIS) data are available to download from https://lpdaac.usgs.gov/, QSCAT radar data from BYU (Brigham Young University) Data Center: https://www.scp.byu.edu/, ALOS PALSAR data from the ALOS Research and Application Project of EORC, JAXA: https://www.eorc.jaxa.jp/ALOS/en/palsar_fnf/fnf_index.htm, All ERA-5 climate data from the ECMWF, the European Center for Medium-Range Weather Forecasts: https://www.ecmwf.int/en/research/climate-reanalysis. The GPP data are available from NASA DAAC: https://daac.ornl.gov/cgi-bin/dsviewer.pl?ds_id=1789, the global biomass data are available from https://doi.org/10.5281/zenodo.4161694, the forest cover change data are available from: http://earthenginepartners.appspot.com/science-2013-global-forest, time series of TC data are available from: https://glad.umd.edu/dataset/long-term-global-land-change. All data and codes used to evaluate the conclusions of the paper and generate the figures and tables are available at https://doi.org/10.5281/zenodo.5083716.

### Datasets used

We selected the tropical and subtropical moist forests (HTFs) as the domain of our study using the WWF ecoregion map[64] (Figure S1). We included tropical and subtropical moist regions in our study area because the exact delineation of the vegetation from wet and evergreen broadleaf forests to moist semi-deciduous broadleaf forests may be difficult across regions. The study domain for the tropical moist forests is more than 2,000 Mha covering all three continents. Unless otherwise noted, all data were reprojected to a 0.1 ° × 0.1 ° latitude-longitude grid (about 120 $km^2$ near the equator). Datasets used in this study span from 1982 to 2018. Unless otherwise noted, we selected this period because it has the most overlap on datasets that are readily available and provide us with a long time series to quantify impacts of climate change and variability on the ecosystem functions.

### Forest stress variables

We selected available datasets to represent LCLUC and climate variables across the tropics. These include TC resulting from deforestation and degradation and forest recovery, and burned areas from forest fire. Climate datasets

include air temperature, VPD, and precipitation. The variables were produced at either monthly or annual time intervals, depending on data availability.

For forest cover change, we used the Advanced Very High-Resolution Radiometer (AVHRR) vegetation continuous fields (VCF) product[6] to represent the forest TC annually. The original dataset provides cover estimates for trees, short vegetation, and bare ground. Because our focus is on tropical forests, we considered only the TC data.

The original dataset spans from 1982 to 2016 and has missing observations in 1994 and 2000. To harmonize and gap-fill the dataset for the entire study period (1982–2018), we leveraged from the overlapped period of AVHRR and MODIS (2001–2016) to build a linear model of TC between MODIS[65] and AVHRR for each pixel. From the linear model, we predicted records for the missing years in 2000, 2017, and 2018 using existing MODIS observations. The missing data in 1994 were gap-filled using the Savitzky-Golay filtering based on neighboring observations in the temporal domain. We also used the Landsat-derived Global Forest Change (GFC) product to identify regions with forest clearing at 30 m spatial resolution.[32] We aggregated the data to obtain the percentage of cleared area at 0.1° × 0.1° resolution for each year with the domain of the HTFs. The total areas in GFC forest clearing (2000–2018) have been calculated to demonstrate the spatial patterns (Figure S3A).

We assumed forest degradation to occur in forest areas that were disturbed by logging, fire, and fragmentation and edge effects,[66] but where forest cover was not completely lost (forest cover >30%). To classify areas as degraded, we developed annual estimates of degradation using data from the pan-tropical degradation project detecting intact forest loss between 2000 and 2013.[67] We set the degradation fraction for each 0.1° × 0.1° pixel calculated from the training data, and applied a machine learning model using boosted trees[68] to produce annual series of degradation (2000–2018). This provides us with the percent of degradation at each grid cell that represents mostly the edge effects from deforestation and roads (including some logging roads) and long-term defoliation that may be the impact of mortality and canopy loss from droughts and understory fires.[67] The final prediction outputs the percentage of degraded area annually from 2000 to 2018 (Figure S3B). We do not expect that the degradation product can accurately capture the effects of selective logging and small-scale shifting cultivations at the large grid cells.

The final forest cover change maps in the HTF domain were based on AVHRR TC time series from 1982 to 2018, with corrections of forest clearing and degradation for the period with observations (2000–2018). Assuming that the forest clearing and degradation observations capture the land-use events correctly, the corrected TC can be

$$TC_c^{(i)} = TC_o^{(i-1)} + \left[TC_o^{(i)} - TC_o^{(i-1)}\right] + D, \quad \text{(Equation 1)}$$

where $TC_c^{(i)}$ is the corrected TC for year $i$, and it equals the sum of original TC from the previous year $TC_o^{(i-1)}$, plus the observed VCF change $[TC_o^{(i)} - TC_o^{(i-1)}]$, and the correction term $D$ due to disturbance events, such as forest clearing and degradation. Although TC observations of earlier years were not corrected, we found the impact of corrections was generally small (1%–3% of the original TC) and disturbances in earlier years were less significant than those in the more recent decades.[69]

For forest fire, we used the time series of the global BA product-based AVHRR LTDR dataset,[70] which covers the period of 1982–2017. It is a monthly dataset with the BA (unit: $m^2$) estimated for each grid cell. We converted the data to areal fraction of BA for the monthly records. The annual sum of BA fraction, in this product, can be higher than 100% for some regions, due to repeated fire events or extensive fires that last longer than a month. However, in our study region of HTF, the BA fraction rarely exceeds 50% in a single year. We added observations in 2018 directly using BA estimates from the MODIS Collection-6 BA data (product name: MCD64A1 v006)[71] to complete the record of BA from 1982 to 2018.

For climate data, we used the monthly air temperature (T) at 2 m above surface data from the ERA5 reanalysis land dataset[72] available from 1981 to 2019 and already at 0.1 ° × 0.1 ° resolution. We calculated the long-term trend using the Mann-Kendall test for the annual mean of each pixel, and normalized the trends (see approach below) only when the trends were statistically significant. Because the amount of water needed by the ecosystem is strongly modulated by temperature and radiation, we used the WB to represent the water stress instead of precipitation anomaly. For any given month $j$, $WB_j$ is defined as the difference between water supply (precipitation, $P_j$) and water loss (temperature- and radiation-dependent potential ET, $PET_j$):

$$WB_j = P_j - PET_j. \quad \text{(Equation 2)}$$

We used the Climate Hazards InfraRed Precipitation with Stations (CHIRPS)[73] monthly rainfall dataset, which combines precipitation estimates from rain gauges and the Tropical Rainfall Measuring Mission Multi-satellite Precipitation Analysis version 7 (TMPA 3B42) to calibrate high-resolution estimates of precipitation from frequent cold cloud duration events from thermal infrared imagery.[73] CHIRPS datasets come at 0.05° resolution, and cover the period from 1981 to present. Similar to the temperature, we normalized the precipitation trends during the driest quarter, and ignored the trends when they were not statistically significant. For the purpose of comparison, we also calculated the rainfall trends for annual mean and driest quarter (Figure S6). Potential evapotranspiration (PET) was obtained from Global Land Evaporation Amsterdam (GLEAM)[74,75] which assimilates a suite of remotely sensed data with a water cycle model. In GLEAM, the evaporation of intercepted water is treated independently of the potential transpiration, but here we considered that PET is the sum of their definition of potential evaporation and the evaporation of intercepted rainfall (i.e., PET = $E_p + E_i$, following the Miralles et al. [2011] notation).[74]

For VPD at 2 m, we used data from the ERA5 reanalysis,[76] developed by the Center for Medium-Range Weather Forecasts (ECMWF) under the Copernicus Climate Change Service (C3S). ERA5 does not provide VPD directly, but temperature ($T^{(a)}$) and dewpoint temperature ($T^{(d)}$) at 2 m. To account for the highly non-linear relationship between temperature and vapor pressure at saturation without relying on hourly data, we estimated VPD for each month $j$ ($VPD_j$) from the mean diurnal cycle of each month:

$$VPD_j = \frac{1}{24}\sum_{h=0}^{23}\left[e\left(T_{hj}^{(a)}\right) - e\left(T_{hj}^{(d)}\right)\right], \quad \text{(Equation 3)}$$

where the index $h$ corresponds to the hour-dependent monthly mean values. The saturation vapor pressure at the given the temperature $e(T)$ is calculated following available empirical equation.[77]

## Forest response variables

We selected four ecosystem response variables related to processes associated with forest carbon cycling. For AGB carbon, we used the recent global live biomass carbon products available for download from (https://doi.org/10.5281/zenodo.4161694) and described in detail in Xu et al.[22] Annual AGB values at 0.1° × 0.1° grid cells from 2000 to 2018 were estimated globally using a large dataset of ground forest inventory plots of multiple censuses (>200,000 plots), systematic airborne lidar scanning data across global tropical forests (>1 Mha) and satellite lidar from Geoscience Laser Altimeter System lidar sampling measurements of vegetation height structure (>8 million samples). To map AGB, we used time series of global wall-to-wall satellite imagery from microwave and optical sensors at 0.1° spatial resolution to improve the sensitivity and uncertainty of AGB estimation globally and across tropics where cloud cover and sensitivity of satellite data at the native satellite resolution makes it difficult to estimate live biomass carbon. The samples from ground and lidar estimates of AGB included variations of forest types (montane, coastal, mangroves, seasonal), environmental conditions (rainfall seasonality and temperature), and regional variations of average wood density. A spatially balanced sampling inventory of AGB is built to train a spatiotemporal machine learning model based on the Random Forest model that predicts AGB and its uncertainty annually from time series of satellite data from a combination microwave (SeaWinds Scatterometer on QuikSCAT, ALOS PALSAR, Shuttle Radar Topography Mission, SRTM) and optical sensors (MODIS visible and thermal bands), and environmental variables, such as the precipitation from Tropical Rainfall Measuring Mission and Global Precipitation Measurement satellites.

For forest GPP, we used recently developed enhanced global GPP from a combination of remote-sensing, climate, and eddy covariance tower observations globally.[78] The enhanced GPP data product is developed from Global Inventory Modeling and Mapping Studies (GIMMS3g) fraction of photosynthetically active radiation record for the period 1982–2016[79] extended by the MODIS data to 2018, and solar-induced chlorophyll fluorescence from the

Global Ozone Monitoring Experiment-2.[80] An optimum light use efficiency (LUE) model previously derived from the global FLUXNET networks[78,81] was used as the primary model to integrate remote-sensing and climate data (VPD, radiation, soil moisture) to estimate long-term (1982–2018) GPP globally at 8-km spatial and biweekly temporal resolutions.

Evapotranspiration (ET) directly quantifies the response of forest water cycling to a combination of forest cover change and climate effects (e.g., droughts).[82] We used the actual evaporation developed from the GLEAM based on its version 3.3a dataset.[74,75] The GLEAM v.3.3a dataset provides global ET estimates derived from a combination of reanalysis, and *in-situ* and satellite data for the period of 1980–2018. The original monthly ET data at 0.25° resolution were spatially interpolated to 0.1° resolution using the cubic spline resampling method to match the resolution of other datasets.

We used MODIS Collection-6 day-time LST data (product name: MOD11A2 v006)[83] to represent radiative heat exchange of the surface. We performed data pre-processing and internal data quality layers were enabled for screening of atmospheric contamination, including cloud cover and aerosol. For each month, we used the median of all available observations after discarding data considered unreliable based on the quality flags. After screening the data for cloud and aerosol effects, we aggregated all clean 1-km pixels to 0.1° grid using spatial average. In cases of missing pixels, we used the multiple imputation by chained equation method[84] for data imputation using nearest observations.

We included the original BI,[85] which estimates how the average abundance of native terrestrial species in a region compares with their abundances before extensive human impacts. Most values of BI range from 0 to 1 (it can exceed 1 in a few regions); higher values indicate regions with higher abundance of species richness. The original index (BI) was for the year 2005 and was updated by including annual forest disturbances.[13] We aggregated the BI data from the original 1-km spatial resolution to 0.1° × 0.1° grid cells and adjusted for changes of forest cover using the most recent data on land-use change and forest structure. First, we weighted each intactness index with the fraction of deforestation from forest cover change data[32] and MODIS BA[86] from 2005 to 2018. Next, we combined the most recent BI index with the Forest Structural Integrity Index (FSII),[87] which includes impacts of human pressure on the forest structural condition. FSII ranges from 0.1 to 18, and the highest values are associated with tall, old-growth forests that experience little human pressure. We scaled FSII by the maximum value to impose a range between 0 and 1 and multiplied the normalized FSII and BI to correct BI for forest structural integrity. The final product provided us with the most recent BI.

### Regional aggregates of stress and response variables

To facilitate a direct comparison of aggregate stress and response variables across continents (Figure 3), we applied a consistent and systematic normalization of the variables.[46,88] The original distribution of each variable $x$ was converted to a Gaussian distribution, using the long-term averages (20 or 37 years depending on the dataset) across all moist tropical forest pixels. We applied a quantile transform, in which the transformation first estimates the cumulative distribution function of the input feature $F(x)$ using a density function $p(x)$ obtained from a non-parametric kernel density estimator:

$$F(x) = \int_{-\infty}^{x} p(x)\, dx. \quad \text{(Equation 4)}$$

The cumulative distribution functions were then converted to normalized $Z$ scores using the quantile function of the standard normal distribution:

$$Z(x) = \sqrt{2}\, erf^{-1}[2\, F(x) - 1], \quad \text{(Equation 5)}$$

where $\text{erf}^{-1}$ is the inverse error function. By performing the non-parametric quantile transformation, we obtained a smoothed-out distribution that is less influenced by outliers than other scaling methods. Finally, we applied the range transformation to scale the values between 0 and 1 as follows:

$$\hat{Z}(x) = \frac{x - \min(x)}{\max(x) - \min(x)}. \quad \text{(Equation 6)}$$

To ensure the consistent impact of each stress and response variable to the environment, we carefully chose the form and direction of each variable for transformation. The variables that applied transformation before comparison were the inverse trend (i.e., negative trends have higher values) of WB ($S_W$) and forest TC ($S_D$), the original long-term trend of temperature ($S_T$) and VPD ($S_V$), and the long-term average for fire ($S_F$) to represent the normalized pattern. We applied the same strategy to response variables, with LST ($R_H$) using the original trend, GPP ($R_P$), ET ($R_E$), and AGB ($R_C$) using the inversed trend, and the long-term mean for BI ($R_B$). The spatially normalized stress and response indices were compared against each other and continentally for relative contributions (wheel charts in Figure 3) when each variable was spatially averaged for each continent.

To present spatial patterns and combined effects of stress and response variables (Figure 3), we applied the weighted linear summation of lower-level normalized variables using weights derived from first-order approximations between stress and response normalized indices:

$$[\![R_k]\!] = \alpha_k + \sum_{c=1}^{N_c} (\beta_c [\![S_c]\!]) + \sum_{h=1}^{N_h} (\beta_h [\![S_h]\!]) + \varepsilon_k. \quad \text{(Equation 7)}$$

For each of the spatially normalized response indices $R_k$ (where $k$ is one of the five response indices used in Figure 3), we built the linear relationship with each of the $N_c = 3$ spatially normalized climate ($S_c$) and $N_h = 2$ human-induced stressors ($S_h$) and found the maximum coefficients that represent the first-order impact from either climate- or human-induced stressors. Building the linear models for each response index, we found the highest first-order impacts of stressors on responses using the maximum coefficients found in five linear models (Figure S7). These coefficients were used as weights to produce upper-level stress indices. For response indices ($R_F$ and $R_S$), we assumed the same contribution from each individual response component, and equal weights were applied to produce upper-level response indices.

### Long-term TFVI

We developed vulnerability indices for any response variable $Y$ (AGB, GPP, ET, LST), using additive autoregressive AR1 models between response and multiple stress variables.[29,46,88] To remove seasonality effects and obtain comparable indices for different response variables, the time series of response variables for each pixel is temporally standardized ($\langle Y \rangle_j$) into $Z$ scores, using month-specific average ($Y_M$) and standard deviation ($\sigma_{YM}$) of the response variable, $M$ being the month of time step $j$. Among climate variables, we selected the WB (Equation 2) and the VPD (Equation 3) to represent the impacts of below- and above-ground water stress on plant physiology, respectively. Although incoming radiation can be an important limiting factor in tropical forests, it also has strong negative correlation with WB. Likewise, air temperature is closely linked to VPD (Equation 3). To account for effects of natural and anthropogenic disturbance, as well as regeneration, we used the forest TC given in terms of fraction area of a pixel. Because only one value of TC per pixel is available for each year, we interpolated the data using a monotone Hermite spline function (function splinefun of the R statistical software).[89,90] Here, we assumed that the annual values were representative of July as a mid-point in the year for which all cloud-free images are used to estimate TC. This interpolation was needed so that we could use it in conjunction with WB and VPD data at the monthly scale.

For each pixel, the response of $\langle Y \rangle$ to climate and disturbance stress is represented by a first-order autoregressive model (AR1):

$$\langle Y \rangle_j = y_0 + \rho_Y \langle Y \rangle_{j-1} + \zeta_{W:Y} \langle \text{WB} \rangle_j + \zeta_{V:Y} \langle \text{VPD} \rangle_j + \zeta_{D:Y} \text{TC}_j + \varepsilon_j, \quad \text{(Equation 8)}$$

where $y_0$ is the intercept, $\langle Y \rangle_{j-1}$ is the standardized response variable in the previous year, $\rho_Y$ is the autocorrelation coefficient of the response variable, $\zeta_{W:Y}$ represents the sensitivity of the response variable to WB, $\zeta_{V:Y}$ represents the sensitivity of the response variable to VPD, $\zeta_{D:Y}$ represents the sensitivity of the response variable to TC, and $\varepsilon_j$ represents the residuals; $\rho_Y$, $\zeta_{W:Y}$, $\zeta_{V:Y}$, and $\zeta_{D:Y}$ are obtained independently for each pixel by fitting a robust linear model using the function rlm of the R statistical software.[91] To obtain the vulnerability index of the response variable ($\text{TFVI}_Y$), we differentiate Equation 8 to quantify changes in the response variable in the long-term (time scale $\Delta t_{LT}$). Because the fitted model is linear, the long-term changes (denoted by $\Delta_{LT}$) in the response variable are also linearly related to the stressors:

$$\frac{\Delta_{LT}\langle Y\rangle_j}{\Delta t_{LT}} = \rho_Y \frac{\Delta_{LT}\langle Y\rangle_{j-1}}{\Delta t_{LT}} + \zeta_{W:Y}\frac{\Delta_{LT}\langle WB\rangle_j}{\Delta t_{LT}} + \zeta_{V:Y}\frac{\Delta_{LT}\langle VPD\rangle_j}{\Delta t_{LT}} + \zeta_{D:Y}\frac{\Delta_{LT}FTC_j}{\Delta t_{LT}} + \frac{\Delta_{LT}\varepsilon_j}{\Delta t_{LT}}. \quad \text{(Equation 9)}$$

Because the fitted AR1 model is unbiased, $\Delta_{LT}\varepsilon_j/\Delta t_{LT} \approx 0$. In addition, if $\Delta t_{LT} \gg 1$ year, we can assume that $\Delta_{LT}\langle Y\rangle_j/\Delta t_{LT} \approx \Delta_{LT}\langle Y\rangle_{j-1}/\Delta t_{LT}$, and simplify the equation above to be:

$$TFVI_Y = \Delta_{LT}\langle Y\rangle = \frac{1}{1-\rho_Y}(\zeta_{W:Y}\,\tau_W + \zeta_{V:Y}\tau_V + \zeta_{D:Y}\tau_D), \quad \text{(Equation 10)}$$

where $\tau_W$, $\tau_V$, and $\tau_D$ are the dimensionless long-term trends of ⟨WB⟩, ⟨VPD⟩, and TC, respectively. To estimate the long-term trend of stress variables, we fitted linear models of the normalized time series, assuming time $t$ to span between $t_a$ (first month of the time series) and $t_z$ (last month of the time series). The long-term trend was assumed to be the fitted slope of the linear model:

$$WB = w_0 + \tau_W\frac{t-t_a}{t_z-t_a}, \quad \text{(Equation 11)}$$

$$VPD = v_0 + \tau_V\frac{t-t_a}{t_z-t_a}, \quad \text{(Equation 12)}$$

$$TC = d_0 + \tau_D\frac{t-t_a}{t_z-t_a}. \quad \text{(Equation 13)}$$

The index $TFVI_Y$ represents the risk of long-term transitions due to increase in stress. For example, if the response variable $Y$ is AGB, negative values of $TFVI_Y$ represent risk of long-term biomass loss. The sensitivity coefficients to climate and disturbance can be either positive or negative; using again the example of biomass, negative values of $\zeta_{W:Y}$, $\zeta_{V:Y}$, or $\zeta_{D:Y}$ mean that increasing stress is associated with biomass loss, and thus more likely to contribute to vulnerability. Spatial variations of sensitivity coefficients demonstrate the links of response variables to different stresses across the tropics (Figures S11–S14). The term $\rho_Y$ is associated with the resilience of the system, and it is typically between zero and one. As described in and shown in Equation 10, values near zero indicate high resilience and the ability of the system to quickly return to equilibrium as long as the product between sensitivity and the long-term trend of any of the stressors is not large (i.e., the numerator of Equation 10 is greater than −1), as the term $1/(1-\rho_Y)$ is approximately 1. In contrast, when $\rho_Y$ values approach 1, anomalies caused even by relatively small anomalies may persist for long periods of time (high vulnerability), as the term $1/(1-\rho_Y) \gg 1$ amplifies the magnitude of such sensitivities, meaning that the system may take longer times to recover. Occasionally, $\rho_Y$ can also be negative, which occurs when the system returns to equilibrium in an oscillatory pattern.[88]

The full model presented in Equations 8 and 10 are used only when the fitted sensitivity coefficients $\zeta_{W:Y}$, $\zeta_{V:Y}$, and $\zeta_{D:Y}$, and the respective long-term trends $\tau_W$, $\tau_V$, and $\tau_D$, are all statistically significant, based on a simple t test at 95% confidence interval. Otherwise, the non-significant coefficients are assumed zero and do not contribute to the vulnerability. In the cases when all sensitivity coefficients are assumed zero, $TFVI_Y$ becomes 0 as per Equation 10, regardless of $\rho_Y$. In addition, when $\rho_Y$ approaches 1, $TFVI_Y$ estimates can become either negatively or positively large. These cases correspond to extreme vulnerability or extreme resilience (depending on the sign of $\zeta_{W:Y}$, $\zeta_{V:Y}$, and $\zeta_{D:Y}$). To facilitate interpretation, we impose lower (−1) and upper bounds (+1) for most $TFVI_Y$ variables. Because we only use annual averages for AGB and the time series is shorter (i.e., less points to fit the model in Equation 8), the model fitting is less robust and results in higher variability of $TFVI_{AGB}$ relative to the other indices. Therefore, we bound the $TFVI_{AGB}$ values to the (−3; +3) interval.

### Uncertainty estimation

Assessment of the uncertainty of TFVI, which is based on a large number of satellite and climate datasets spanning multiple decades is a challenging problem. To determine the uncertainty in patterns of vulnerability represented in TFVIs of different responses, we use an error propagation approach to propagate the errors associated with the stress and response variables and the AR1 model to TFVI. Among stress variables used in the model, the climate data are derived from model reanalysis are often not accompanied by errors. All remote-sensing-based data products on the other hand include uncertainty estimates either at the pixel level or on the overall products using a variety of methods (Table S2). For TFVI we used two climate variables (WB, VPD) and one LCLUC variable (TC). For response variables GPP and ET, we found the production validation and prediction error insufficient and adopted the method of triple collocation[92,93] for estimating pixel level uncertainty when several similar type products are available. The triple collocation technique takes three spatially and temporally collocated estimates of the same variable to solve a set of equations related to the temporal covariance of the estimates from different products. Building on the assumption that we have zero covariance terms for both residual errors between products, and between errors and truth, the pixel level error for each product can be expressed using sample covariance matrices between participating products. We therefore estimated the GPP uncertainty of the enhanced GPP data product[78] using two other independent GPP products, GOSIF[94] and FluxCom,[95] for the overlapped period (2002–2015) to form the triplets. To estimate the uncertainty of ET, we collected additional ET products from ERA5 and MODIS and used the GLEAM ET from our study to perform triple collocation for the overlapped period (2002–2018). The biomass carbon AGB data were accompanied by pixel level uncertainty estimates, and the LST products from MODIS also included an overall average uncertainty.[83]

The TFVI estimation from the AR1 model also has sources of uncertainty from errors in input layers (error from satellite data), and errors in fitting the model (Equation 8). The errors in satellite data layers, when focusing on the long-term trend, are associated with the standard errors of trend values ($\sigma_\tau$). The model-related uncertainty, which consists of parameter uncertainty ($\sigma_P$) and the AR1 model residual errors were propagated to long-term trends ($\sigma_{\varepsilon,LT}$) using the hybrid inferences[96,97]:

$$\sigma^2_{TFVI} = \sigma^2_\tau + \sigma^2_P + \sigma^2_{\varepsilon,\,LT}. \quad \text{(Equation 14)}$$

The uncertainty associated with long-term trends of stressors can be estimated using standard error propagation, assuming that the uncertainty of long-term trends are not correlated with the construction of AR1 model:

$$\sigma^2_\tau = \left(\frac{\zeta_{W:Y}}{1-\rho_Y}\right)^2\sigma^2_{\tau_W} + \left(\frac{\zeta_{V:Y}}{1-\rho_Y}\right)^2\sigma^2_{\tau_V} + \left(\frac{\zeta_{D:Y}}{1-\rho_Y}\right)^2\sigma^2_{\tau_D}, \quad \text{(Equation 15)}$$

where $\sigma^2_{\tau_V}$ and $\sigma^2_{\tau_D}$ are the parameter estimation standard errors of Equations 11, 12, 13.

The parameter uncertainty can be approximated using the first-order Taylor expansion[98,99]:

$$\sigma^2_P = \sum_{q=1}^{4}\sum_{q'=1}^{4}\left[\frac{\partial TFVI}{\partial p_q}\frac{\partial TFVI}{\partial p_{q'}}\mathrm{cov}(p_q, p_{q'})\right], \quad \text{(Equation 16)}$$

where $p_q$ corresponds to each parameter of the AR1 model included in the derivation of TFVI, (namely $\zeta_{W:Y}$, $\zeta_{W:Y}$, $\zeta_{W:Y}$, and $\rho_Y$).

The model residual error propagated to long-term trends is represented by the variance of the long-term trend of residuals, i.e., $\sigma^2_{\varepsilon,LT} = \mathrm{var}\left(\frac{\Delta_{LT}\varepsilon}{\Delta t_{LT}}\right)$. Assuming that the residuals of the AR1 are independent of time, the long-term trend can be translated to the mean of first differences of $N_t$ observations and the corresponding $\sigma_{\varepsilon,LT}$ is equivalent to the uncertainty of the long-term average of the model prediction uncertainty obtained from Equation 8 ($\sigma_{AR1}$):

$$\sigma^2_{\varepsilon,LT} = \left(\frac{1}{1-\rho}\right)^2\frac{2\sigma^2_{AR1}}{N_t-1}. \quad \text{(Equation 17)}$$

## SUPPLEMENTAL INFORMATION

Supplemental information can be found online at https://doi.org/10.1016/j.oneear.2021.06.002.

## ACKNOWLEDGMENTS

This project was organized by the National Geographic Society and supported by Rolex as part of its Perpetual Planet initiative. A convening to bring together all co-authors took place at National Geographic headquarters in October

2019, to formulate this work; we thank Jonathan Baillie for helpful ideas on structuring the work and convening, Alexis Bahl for logistics and support, Erin Martin for facilitating, and Sandra Elvin for helpful comments on an earlier draft. Part of this work was carried out at the Jet Propulsion Laboratory, California Institute of Technology, under a contract with the National Aeronautics and Space Administration (NASA). Y.Y. and M.L. were supported by the NASA Postdoctoral Program, administered by Universities Space Research Association under contract with NASA; L.X. was partially supported by NASA's Terrestrial Ecology and Carbon Cycle (16-CARBON16-0130) and S.S. by NASA's Interdisciplinary Science program (N6-IDS16-0059).

## AUTHOR CONTRIBUTIONS

S.S. conceived the idea. S.S., M.L., L.X., and Y.Y. designed the research and performed the analysis. S.S. wrote the main manuscript. M.L., L.X., and Y.Y. wrote the methods and the supplementary information. A.E. directed the study, and reviewed and commented on paper. All authors reviewed and edited the paper.

## DECLARATION OF INTERESTS

The authors declare no competing interests.

Received: January 14, 2021
Revised: March 28, 2021
Accepted: June 9, 2021
Published: July 23, 2021

## REFERENCES

1. Malhi, Y., Gardner, T.A., Goldsmith, G.R., Silman, M.R., and Zelazowski, P. (2014). Tropical forests in the Anthropocene. Annu. Rev. Environ. Resour. *39*, 125–159.
2. Trumbore, S., Brando, P., and Hartmann, H. (2015). Forest health and global change. Science (80- *349*, 814–818.
3. Lewis, S.L., Edwards, D.P., and Galbraith, D. (2015). Increasing human dominance of tropical forests. Science *349*, 827–832.
4. Wright, J.S., Fu, R., Worden, J.R., Chakraborty, S., Clinton, N.E., Risi, C., Sun, Y., and Yin, L. (2017). Rainforest-initiated wet season onset over the southern Amazon. Proc. Natl. Acad. Sci. U. S. A. *114*, 8481–8486.
5. Zhou, L., Tian, Y., Myneni, R.B., Ciais, P., Saatchi, S., Liu, Y.Y., Piao, S., Chen, H., Vermote, E.F., Song, C., et al. (2014). Widespread decline of Congo rainforest greenness in the past decade. Nature *508*, 86–90.
6. Song, X.P., Hansen, M.C., Stehman, S.V., Potapov, P.V., Tyukavina, A., Vermote, E.F., and Townshend, J.R. (2018). Global land change from 1982 to 2016. Nature *560*, 639–643.
7. Saatchi, S., Asefi-Najafabady, S., Malhi, Y., Aragão, L.E.O.C., Anderson, L.O., Myneni, R.B., and Nemani, R. (2013). Persistent effects of a severe drought on Amazonian forest canopy. Proc. Natl. Acad. Sci. U. S. A. *110*, 565–570.
8. Vancutsem, C., Achard, F., Pekel, J.-F., Vieilledent, G., Carboni, S., Simonetti, D., Gallego, J., Aragão, L.E.O.C., and Nasi, R. (2021). Long-term (1990–2019) monitoring of forest cover changes in the humid tropics. Sci. Adv. *7*, eabe1603.
9. Yang, Y., Saatchi, S.S., Xu, L., Yu, Y., Choi, S., Phillips, N., Kennedy, R., Keller, M., Knyazikhin, Y., and Myneni, R.B. (2018). Post-drought decline of the Amazon carbon sink. Nat. Comm. *9*, 3172.
10. Aleixo, I., Norris, D., Hemerik, L., Barbosa, A., Prata, E., Costa, F., and Poorter, L. (2019). Amazonian rainforest tree mortality driven by climate and functional traits. Nat. Clim. Chang. *9*, 384–388.
11. Harris, N.L., Gibbs, D.A., Baccini, A., Birdsey, R.A., de Bruin, S., Farina, M., Fatoyinbo, L., Hansen, M.C., Herold, M., Houghton, R.A., et al. (2021). Global maps of twenty-first century forest carbon fluxes. Nat. Clim. Chang. *11*, 234–240.
12. Longo, M., Saatchi, S., Keller, M., Bowman, K., Ferraz, A., Moorcroft, P.R., Morton, D.C., Bonal, D., Brando, P., Burban, B., et al. (2020). Impacts of degradation on water, energy, and carbon cycling of the Amazon tropical forests. J. Geophys. Res. Biogeosciences *125*. https://doi.org/10.1029/2020JG005677.
13. Palma, A. De, Hoskins, A., Gonzalez, R.E., Börger, L., Newbold, T., Sanchez-Ortiz, K., Ferrier, S., and Purvis, A. (2019). Changes in the Biodiversity Intactness Index in tropical and subtropical forest biomes, 2001–2012. bioRxiv, 311688.
14. Lewis, S. (2006). Tropical forests and the changing earth system. Phil Trans. R. Soc. B *361*, 195–210.
15. Nobre, C.A., Sampaio, G., Borma, L.S., Castilla-Rubio, J.C., Silva, J.S., and Cardoso, M. (2016). Land-use and climate change risks in the amazon and the need of a novel sustainable development paradigm. Proc. Natl. Acad. Sci. U. S. A. *113*, 10759–10768.
16. Malhi, Y., Aragão, L.E.O.C., Galbraith, D., Huntingford, C., Fisher, R., Zelazowski, P., Sitch, S., McSweeney, C., and Meir, P. (2009). Exploring the likelihood and mechanism of a climate-change-induced dieback of the Amazon rainforest. Proc. Natl. Acad. Sci. U. S. A. *106*, 20610–20615.
17. Levine, N.M., Zhang, K., Longo, M., Baccini, A., Phillips, O.L., Lewis, S.L., Alvarez-Dávila, E., De Andrade, A.C.S., Brienen, R.J.W., Erwin, T.L., et al. (2016). Ecosystem heterogeneity determines the ecological resilience of the Amazon to climate change. Proc. Natl. Acad. Sci. U. S. A. *113*, 793–797.
18. Huntingford, C., Zelazowski, P., Galbraith, D., Mercado, L.M., Sitch, S., Fisher, R., Lomas, M., Walker, A.P., Jones, C.D., Booth, B.B.B., et al. (2013). Simulated resilience of tropical rainforests to $CO_2$-induced climate change. Nat. Geosci. *6*, 268–273.
19. Cox, P.M., Pearson, D., Booth, B.B., Friedlingstein, P., Huntingford, C., Jones, C.D., and Luke, C.M. (2013). Sensitivity of tropical carbon to climate change constrained by carbon dioxide variability. Nature *494*, 341–344.
20. Phillips, O.L., Aragão, L.E.O.C., Lewis, S.L., Fisher, J.B., Lloyd, J., López-González, G., Malhi, Y., Monteagudo, A., Peacock, J., Quesada, C.A., et al. (2009). Drought sensitivity of the amazon rainforest. Science *323*, 1344–1347.
21. Cole, L.E.S., Bhagwat, S.A., and Willis, K.J. (2014). Recovery and resilience of tropical forests after disturbance. Nat. Commun. *5*, 1–7.
22. Xu, L., Saatchi, S., Yang, Y., et al. (2021). Changes in Global Terrestrial Live Biomass Over the 21st Century. Sci. Adv. *7* (27), eabe9829. https://doi.org/10.1126/sciadv.abe9829.
23. Jin, M., and Dickinson, R.E. (2010). Land surface skin temperature climatology: benefitting from the strengths of satellite observations. Environ. Res. Lett. *5*, 044004.
24. Turner, B.L., Kasperson, R.E., Matsone, P.A., McCarthy, J.J., Corell, R.W., Christensene, L., Eckley, N., Kasperson, J.X., Luers, A., Martello, M.L., et al. (2003). A framework for vulnerability analysis in sustainability science. Proc. Natl. Acad. Sci. U. S. A. *100*, 8074–8079.
25. Folke, C., Carpenter, S., Walker, B., Scheffer, M., Elmqvist, T., Gunderson, L., and Holling, C.S. (2004). Regime shifts, resilience, and biodiversity in ecosystem management. Annu. Rev. Ecol. Evol. Syst. *35*, 557–581.
26. Williams, L.R.R., and Kapustka, L.A. (2000). Ecosystem vulnerability: a complex interface with technical components. Environ. Toxicol. Chem. *19*, 1055–1058.
27. Dakos, V., Van Nes, E.H., D'Odorico, P., and Scheffer, M. (2012). Robustness of variance and autocorrelation as indicators of critical slowing down. Ecology *93*, 264–271.
28. Scheffer, M., Bascompte, J., Brock, W.A., Brovkin, V., Carpenter, S.R., Dakos, V., Held, H., Van Nes, E.H., Rietkerk, M., and Sugihara, G. (2009). Early-warning signals for critical transitions. Nature *461*, 53–59.
29. Verbesselt, J., Umlauf, N., Hirota, M., Holmgren, M., Van Nes, E.H., Herold, M., Zeileis, A., and Scheffer, M. (2016). Remotely sensed resilience of tropical forests. Nat. Clim. Chang. *6*, 1028–1031.
30. Seddon, N., Chausson, A., Berry, P., Girardin, C.A.J., Smith, A., and Turner, B. (2020). Understanding the value and limits of nature-based

solutions to climate change and other global challenges. Philos. Trans. R. Soc. B Biol. Sci. *375*. https://doi.org/10.1098/rstb.2019.0120.

31. Curtis, P.G., Slay, C.M., Harris, N.L., Tyukavina, A., and Hansen, M.C. (2018). Classifying drivers of global forest loss. Science *361*, 1108–1111.
32. Hansen, M.C., Potapov, P.V., Moore, R., Hancher, M., Turubanova, S.A., Tyukavina, A., Thau, D., Stehman, S.V., Goetz, S.J., Loveland, T.R., et al. (2013). High-resolution global maps of 21st-century forest cover change. Science (80-. ) *342*, 850–853.
33. Smith, M.N., Taylor, T.C., van Haren, J., Rosolem, R., Restrepo-Coupe, N., Adams, J., Wu, J., de Oliveira, R.C., da Silva, R., de Araujo, A.C., et al. (2020). Empirical evidence for resilience of tropical forest photosynthesis in a warmer world. Nat. Plants *6*, 1225–1230.
34. Barkhordarian, A., Saatchi, S.S., Behrangi, A., Loikith, P.C., and Mechoso, C.R. (2019). A recent systematic increase in vapor pressure deficit over Tropical South America. Sci. Rep. *9*, 1–12.
35. Marengo, J.A., Williams, E.R., Alves, L.M., Soares, W.R., and Rodriguez, D.A. (2016). Extreme seasonal climate variations in the Amazon Basin: droughts and floods. In Interactions between Biosphere, Atmosphere and Human Land Use in the Amazon Basin (Springer), pp. 55–76.
36. Asefi-Najafabady, S., and Saatchi, S. (2013). Response of African humid tropical forests to recent rainfall anomalies. Philos. Trans. R. Soc. Lond. B. Biol. Sci. *368*, 20120306.
37. Hubau, W., Lewis, S.L., Phillips, O.L., Affum-Baffoe, K., Beeckman, H., Cuní-Sanchez, A., Daniels, A.K., Ewango, C.E.N., Fauset, S., Mukinzi, J.M., et al. (2020). Asynchronous carbon sink saturation in African and Amazonian tropical forests. Nature *579*, 80–87.
38. Tong, X., Brandt, M., Yue, Y., Ciais, P., Rudbeck Jepsen, M., Penuelas, J., Wigneron, J.-P., Xiao, X., Song, X.-P., Horion, S., et al. (2020). Forest management in southern China generates short term extensive carbon sequestration. Nat. Commun. *11*, 129.
39. Zhang, Y., Song, C., Band, L.E., and Sun, G. (2019). No proportional increase of terrestrial gross carbon sequestration from the greening Earth. J. Geophys. Res. Biogeosciences *124*, 2540–2553.
40. Gloor, M., Brienen, R.J.W., Galbraith, D., Feldpausch, T.R., Schöngart, J., Guyot, J.L., Espinoza, J.C., Lloyd, J., and Phillips, O.L. (2013). Intensification of the Amazon hydrological cycle over the last two decades. Geophys. Res. Lett. *40*, 1729–1733.
41. Gerken, T., Ruddell, B.L., Fuentes, J.D., Araújo, A., Brunsell, N.A., Maia, J., Manzi, A., Mercer, J., dos Santos, R.N., von Randow, C., et al. (2017). Investigating the mechanisms responsible for the lack of surface energy balance closure in a central Amazonian tropical rainforest. Agric. For. Meteorol.
42. Bittencourt, P.R.L., Oliveira, R.S., da Costa, A.C.L., Giles, A.L., Coughlin, I., Costa, P.B., Bartholomew, D.C., Ferreira, L.V., Vasconcelos, S.S., Barros, F.V., et al. (2020). Amazonia trees have limited capacity to acclimate plant hydraulic properties in response to long-term drought. Glob. Chang. Biol. *26*, 3569–3584.
43. Choat, B., Jansen, S., Brodribb, T.J., Cochard, H., Delzon, S., Bhaskar, R., Bucci, S.J., Feild, T.S., Gleason, S.M., Hacke, U.G., et al. (2012). Global convergence in the vulnerability of forests to drought. Nature *491*, 752–755.
44. Meir, P., and Woodward, F.I. (2010). Amazonian rain forests and drought: response and vulnerability. New Phytol. *187*, 553–557.
45. Longo, M., Knox, R.G., Levine, N.M., Alves, L.F., Bonal, D., Camargo, P.B., Fitzjarrald, D.R., Hayek, M.N., Restrepo-Coupe, N., Saleska, S.R., et al. (2018). Ecosystem heterogeneity and diversity mitigate Amazon forest resilience to frequent extreme droughts. New Phytol. *219*, 914–931.
46. Seddon, A.W.R., Macias-Fauria, M., Long, P.R., Benz, D., and Willis, K.J. (2016). Sensitivity of global terrestrial ecosystems to climate variability. Nature *531*, 229–232.
47. Hirota, M., Holmgren, M., Van Nes, E.H., and Scheffer, M. (2011). Global resilience of tropical forest and savanna to critical transitions. Science (80-. ) *334*, 232–235.
48. M. Bush, J. Flenley, and W. Gosling, eds. (2011). Tropical Rainforest Responses to Climatic Change (Springer Berlin Heidelberg).
49. França, F.M., Benkwitt, C.E., Peralta, G., Robinson, J.P.W., Graham, N.A.J., Tylianakis, J.M., Berenguer, E., Lees, A.C., Ferreira, J., Louzada, J., et al. (2020). Climatic and local stressor interactions threaten tropical forests and coral reefs. Philos. Trans. R. Soc. B Biol. Sci. *375*, 20190116.
50. Nolan, C., Overpeck, J.T., Allen, J.R.M., Anderson, P.M., Betancourt, J.L., Binney, H.A., Brewer, S., Bush, M.B., Chase, B.M., Cheddadi, R., et al. (2018). Past and future global transformation of terrestrial ecosystems under climate change. Science, 361.
51. Bauters, M., Meeus, S., Barthel, M., Stoffelen, P., De Deurwaerder, H.P.T., Meunier, F., Drake, T.W., Ponette, Q., Ebuy, J., Vermeir, P., et al. (2020). Century-long apparent decrease in intrinsic water-use efficiency with no evidence of progressive nutrient limitation in African tropical forests. Glob. Chang. Biol. *26*, 4449–4461.
52. Slik, J.W.F., Franklin, J., Arroyo-Rodríguez, V., Field, R., Aguilar, S., Aguirre, N., Ahumada, J., Aiba, S.-I., Alves, L.F., K, A., et al. (2018). Phylogenetic classification of the world's tropical forests. Proc. Natl. Acad. Sci. U S A *115*, 1837–1842. https://doi.org/10.1073/pnas.1714977115.
53. Parmentier, I., Malhi, Y., Senterre, B., Whittaker, R.J., N, A.T.N., Alonso, A., Balinga, M.P.B., Bakayoko, A., Bongers, F., Chatelain, C., et al. (2007). The odd man out? Might climate explain the lower tree $\alpha$-diversity of African rain forests relative to Amazonian rain forests? J. Ecol. *95*, 1058–1071.
54. Schmitt, S., Maréchaux, I., Chave, J., Fischer, F.J., Piponiot, C., Traissac, S., and Hérault, B. (2019). Functional diversity improves tropical forest resilience: insights from a long-term virtual experiment. J. Ecol.
55. Ordway, E.M., Asner, G.P., and Lambin, E.F. (2017). Deforestation risk due to commodity crop expansion in sub-Saharan Africa. Environ. Res. Lett. *12*. https://doi.org/10.1088/1748-9326/aa6509.
56. Costa, M.H., and Foley, J.A. (2000). Combined effects of deforestation and doubled atmospheric $CO_2$ concentrations on the climate of Amazonia. J. Clim. *13*, 18–34.
57. Rowland, L., Da Costa, A.C.L., Galbraith, D.R., Oliveira, R.S., Binks, O.J., Oliveira, A.A.R., Pullen, A.M., Doughty, C.E., Metcalfe, D.B., Vasconcelos, S.S., et al. (2015). Death from drought in tropical forests is triggered by hydraulics not carbon starvation. Nature *528*, 119–122.
58. Brienen, R.J.W., Phillips, O.L., Feldpausch, T.R., Gloor, E., Baker, T.R., Lloyd, J., Lopez-Gonzalez, G., Monteagudo-Mendoza, A., Malhi, Y., Lewis, S.L., et al. (2015). Long-term decline of the Amazon carbon sink. Nature *519*, 344–348.
59. Brienen, R.J.W., Schöngart, J., and Zuidema, P.A. (2016). Tree rings in the tropics: insights into the ecology and climate sensitivity of tropical trees. In Tree Physiology (Springer), pp. 439–461.
60. oppenheimer, m., campos, m., warren, r., birkmann, j., lubbe, g., o'neill, b., and takahashi, K. (2015). Emergent risks and key vulnerabilities. In Climate Change 2014 Impacts, Adaptation, and Vulnerability, C.B. Field, V.R. Barros, D.J. Dokken, K.J. Mach, and M.D. Mastrandrea, eds. (Cambridge University Press), pp. 1039–1100.
61. Dakos, V., Scheffer, M., Van Nes, E.H., Brovkin, V., Petoukhov, V., and Held, H. (2008). Slowing down as an early warning signal for abrupt climate change. Proc. Natl. Acad. Sci. U. S. A. *105*, 14308–14312.
62. Chen, Y., Randerson, J.T., Coffield, S.R., Foufoula-Georgiou, E., Smyth, P., Graff, C.A., Morton, D.C., Andela, N., Werf, G.R., Giglio, L., et al. (2020). Forecasting global fire emissions on subseasonal to seasonal (S2S) time scales. J. Adv. Model. Earth Syst. *12*. https://doi.org/10.1029/2019MS001955.
63. Chun, K.P., Wheater, H., and Onof, C. (2013). Prediction of the impact of climate change on drought: an evaluation of six UK catchments using two stochastic approaches. Hydrol. Process. *27*, 1600–1614.
64. Olson, D. (2001). Terrestrial ecoregions of the world: a new map of life on Earth: a new global map of terrestrial ecoregions provides an innovative tool for conserving biodiversity. Bioscience *51*, 933–938.
65. DiMiceli, C., Townshend, J., Carroll, M., and Sohlberg, R. (2021). Evolution of the representation of global vegetation by vegetation continuous fields. Remote Sensing of Environment *254*, 112271.

66. Hosonuma, N., Herold, M., De Sy, V., De Fries, R.S., Brockhaus, M., Verchot, L., Angelsen, A., and Romijn, E. (2012). An assessment of deforestation and forest degradation drivers in developing countries. Environ. Res. Lett. *7*, 044009.

67. Maxwell, S.L., Evans, T., Watson, J.E.M., Morel, A., Grantham, H., Duncan, A., Harris, N., Potapov, P., Runting, R.K., Venter, O., et al. (2019). Degradation and forgone removals increase the carbon impact of intact forest loss by 626%. Sci. Adv. *5*. https://doi.org/10.1126/sciadv.aax2546.

68. Chen, T., and Guestrin, C. (2016). XGBoost: a scalable tree boosting system. In Proceedings of the ACM SIGKDD International Conference on Knowledge Discovery and Data Mining (Association for Computing Machinery), pp. 785–794.

69. Rosa, I.M.D., Smith, M.J., Wearn, O.R., Purves, D., and Ewers, R.M. (2016). The environmental legacy of modern tropical deforestation. Curr. Biol. *26*, 2161–2166.

70. Otón, G., Ramo, R., Lizundia-Loiola, J., and Chuvieco, E. (2019). Global detection of long-term (1982–2017) burned area with AVHRR-LTDR data. Remote Sens *11*, 2079.

71. Giglio, L., Boschetti, L., Roy, D.P., Humber, M.L., and Justice, C.O. (2018). The Collection 6 MODIS burned area mapping algorithm and product. Remote Sens. Environ. *217*, 72–85.

72. Hersbach, H., Bell, B., Berrisford, P., Hirahara, S., Horányi, A., Muñoz-Sabater, J., Nicolas, J., Peubey, C., Radu, R., Schepers, D., et al. (2020). The ERA5 global reanalysis. Q. J. R. Meteorol. Soc. *146*, 1999–2049.

73. Funk, C., Peterson, P., Landsfeld, M., Pedreros, D., Verdin, J., Shukla, S., Husak, G., Rowland, J., Harrison, L., Hoell, A., et al. (2015). The climate hazards infrared precipitation with stations—a new environmental record for monitoring extremes. Sci. Data *2*. https://doi.org/10.1038/sdata.2015.66.

74. Miralles, D.G., Holmes, T.R.H., De Jeu, R.A.M., Gash, J.H., Meesters, A.G.C.A., and Dolman, A.J. (2011). Global land-surface evaporation estimated from satellite-based observations. Hydrol. Earth Syst. Sci. *15*, 453–469.

75. Martens, B., Miralles, D.G., Lievens, H., Van Der Schalie, R., De Jeu, R.A.M., Fernández-Prieto, D., Beck, H.E., Dorigo, W.A., and Verhoest, N.E.C. (2017). GLEAM v3: satellite-based land evaporation and root-zone soil moisture. Geosci. Model Dev. *10*, 1903–1925.

76. Hersbach, H., Bell, B., Berrisford, P., Hirahara, S., Horányi, A., Muñoz-Sabater, J., Nicolas, J., Peubey, C., Radu, R., Schepers, D., et al. (2020). The ERA5 global reanalysis. Q. J. R. Meteorol. Soc. *146*, 1999–2049.

77. Murphy, D.M., and Koop, T. (2005). Review of the vapour pressures of ice and supercooled water for atmospheric applications. Quart. J. R. Meteorol. Soc. *131*, 1539–1565.

78. Madani, N., Parazoo, N.C., Kimball, J.S., Ballantyne, A.P., Reichle, R.H., Maneta, M., Saatchi, S., Palmer, P.I., Liu, Z., and Tagesson, T. (2020). Recent amplified global gross primary productivity due to temperature increase is offset by reduced productivity due to water constraints. Agu Adv. https://doi.org/10.1029/2020AV000180.

79. Zhu, Z., Bi, J., Pan, Y., Ganguly, S., Anav, A., Xu, L., Samanta, A., Piao, S., Nemani, R.R., and Myneni, R.B. (2013). Global data sets of vegetation leaf area index (LAI)3g and fraction of photosynthetically active radiation (FPAR)3g derived from global inventory modeling and mapping studies (GIMMS) normalized difference vegetation index (NDVI3G) for the period 1981 to 2011. Remote Sens *5*, 927–948.

80. Köhler, P., Guanter, L., and Joiner, J. (2015). A linear method for the retrieval of sun-induced chlorophyll fluorescence from GOME-2 and SCIAMACHY data. Atmos. Meas. Tech. *8*, 2589–2608.

81. Madani, N., Kimball, J.S., and Running, S.W. (2017). Improving global gross primary productivity estimates by computing optimum light use efficiencies using flux tower data. J. Geophys. Res. Biogeosciences *122*, 2939–2951.

82. Swann, A.L.S., Hoffman, F.M., Koven, C.D., and Randerson, J.T. (2016). Plant responses to increasing $CO_2$ reduce estimates of climate impacts on drought severity. Proc. Natl. Acad. Sci. U. S. A. *113*, 10019–10024.

83. Wan, Z., Hook, S., and Hulley, G. (2015). MOD11A2 MODIS/Terra land surface temperature/emissivity 8-day L3 global 1km SIN grid V006. NASA EOSDIS Land Processes DAAC *10*.

84. Azur, M.J., Stuart, E.A., Frangakis, C., and Leaf, P.J. (2011). Multiple imputation by chained equations: what is it and how does it work? Int. J. Methods Psychiatr. Res. *20*, 40–49.

85. Newbold, T., Hudson, L.N., Arnell, A.P., Contu, S., De Palma, A., Ferrier, S., Hill, S.L.L., Hoskins, A.J., Lysenko, I., Phillips, H.R.P., et al. (2016). Has land use pushed terrestrial biodiversity beyond the planetary boundary? A global assessment. Science (80-. ) *353*, 291–298.

86. Giglio, L., Schroeder, W., and Justice, C.O. (2016). The collection 6 MODIS active fire detection algorithm and fire products. Remote Sensing of Environment *178*, 31–41.

87. Hansen, A., Barnett, K., Jantz, P., Phillips, L., Goetz, S.J., Hansen, M., Venter, O., Watson, J.E.M., Burns, P., Atkinson, S., et al. (2019). Global humid tropics forest structural condition and forest structural integrity maps. Sci. Data *6*, 232.

88. De Keersmaecker, W., Lhermitte, S., Tits, L., Honnay, O., Somers, B., and Coppin, P. (2015). A model quantifying global vegetation resistance and resilience to short-term climate anomalies and their relationship with vegetation cover. Glob. Ecol. Biogeogr. *24*, 539–548.

89. Fritsch, F.N., and Carlson, R.E. (1980). Monotone piecewise cubic interpolation. SIAM J. Numer. Anal. *17*, 238–246.

90. R Core Team. http://www.R-project.

91. Venables, W.N., and Ripley, B.D. (2002). Random and mixed effects (Springer), pp. 271–300.

92. Alemohammad, S.H., McColl, K.A., Konings, A.G., Entekhabi, D., and Stoffelen, A. (2015). Characterization of precipitation product errors across the United States using multiplicative triple collocation. Hydrol. Earth Syst. Sci. *19*, 3489–3503.

93. McColl, K.A., Vogelzang, J., Konings, A.G., Entekhabi, D., Piles, M., and Stoffelen, A. (2014). Extended triple collocation: estimating errors and correlation coefficients with respect to an unknown target. Geophys. Res. Lett. *41*, 6229–6236.

94. Li, X., and Xiao, J. (2019). A global, 0.05-degree product of solar-induced chlorophyll fluorescence derived from OCO-2, MODIS, and reanalysis data. Remote Sens *11*, 517.

95. Jung, M., Schwalm, C., Migliavacca, M., Walther, S., Camps-Valls, G., Koirala, S., Anthoni, P., Besnard, S., Bodesheim, P., Carvalhais, N., et al. (2020). Scaling carbon fluxes from eddy covariance sites to globe: synthesis and evaluation of the FLUXCOM approach. Biogeosciences *17*, 1343–1365.

96. McRoberts, R.E., Chen, Q., Domke, G.M., Ståhl, G., Saarela, S., and Westfall, J.A. (2016). Hybrid estimators for mean aboveground carbon per unit area. For. Ecol. Manage. *378*, 44–56.

97. Chen, Q., Laurin, G.V., and Valentini, R. (2015). Uncertainty of remotely sensed aboveground biomass over an African tropical forest: propagating errors from trees to plots to pixels. Remote Sens. Environ. *160*, 134–143.

98. Chen, Q., McRoberts, R.E., Wang, C., and Radtke, P.J. (2016). Forest aboveground biomass mapping and estimation across multiple spatial scales using model-based inference. Remote Sens. Environ. *184*, 350–360.

99. Ståhl, G., Holm, S., Gregoire, T.G., Gobakken, T., Næsset, E., and Nelson, R. (2011). Model-based inference for biomass estimation in a LiDAR sample survey in Hedmark County, Norway. This article is one of a selection of papers from extending forest inventory and monitoring over space and time. Can. J. For. Res. *41*, 96–107.

**One Earth, Volume *4***

## Supplemental information

# Detecting vulnerability of humid tropical forests to multiple stressors

**Sassan Saatchi, Marcos Longo, Liang Xu, Yan Yang, Hitofumi Abe, Michel André, Juliann E. Aukema, Nuno Carvalhais, Hinsby Cadillo-Quiroz, Gillian Ann Cerbu, Janet M. Chernela, Kristofer Covey, Lina María Sánchez-Clavijo, Isai V. Cubillos, Stuart J. Davies, Veronique De Sy, Francois De Vleeschouwer, Alvaro Duque, Alice Marie Sybille Durieux, Kátia De Avila Fernandes, Luis E. Fernandez, Victoria Gammino, Dennis P. Garrity, David A. Gibbs, Lucy Gibbon, Gae Yansom Gowae, Matthew Hansen, Nancy Lee Harris, Sean P. Healey, Robert G. Hilton, Christine May Johnson, Richard Sufo Kankeu, Nadine Therese Laporte-Goetz, Hyongki Lee, Thomas Lovejoy, Margaret Lowman, Raymond Lumbuenamo, Yadvinder Malhi, Jean-Michel M. Albert Martinez, Carlos Nobre, Adam Pellegrini, Jeremy Radachowsky, Francisco Román, Diane Russell, Douglas Sheil, Thomas B. Smith, Robert G.M. Spencer, Fred Stolle, Hesti Lestari Tata, Dennis del Castillo Torres, Raphael Muamba Tshimanga, Rodrigo Vargas, Michelle Venter, Joshua West, Atiek Widayati, Sylvia N. Wilson, Steven Brumby, and Aurora C. Elmore**

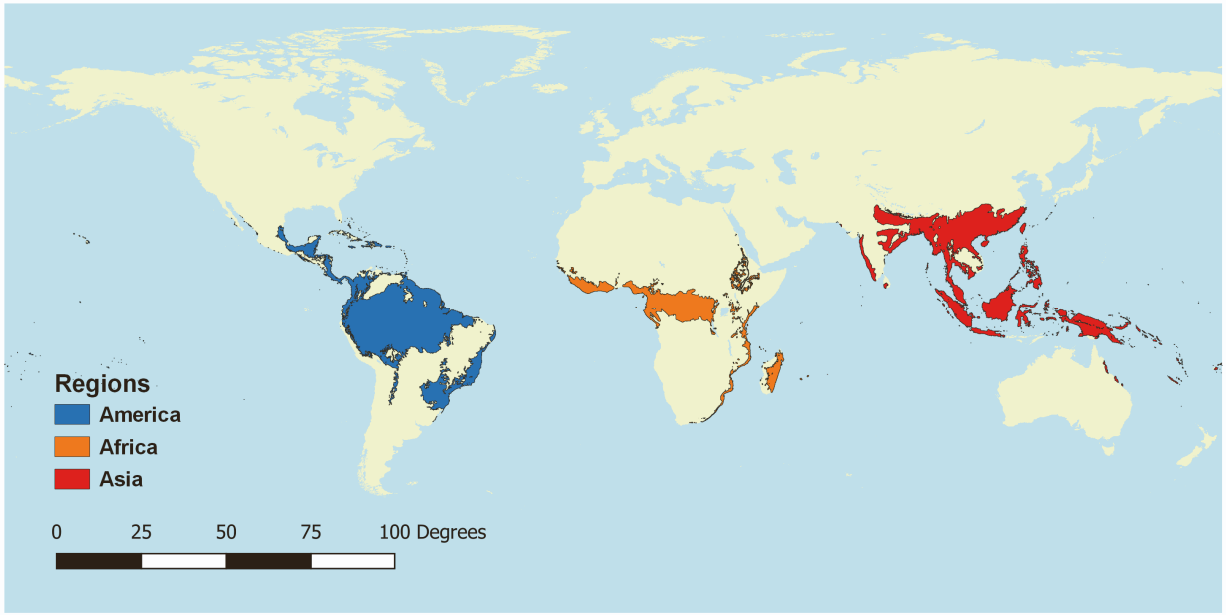


**Figure S1. Tropical/Sub-Tropical moist forests**. The regions were defined from the WWF eco-region map[1]. We included tropical and subtropical moist ecoregions in our study, and separated the study region by continents. The original vector product was rasterized to the 0.1°×0.1° grid.

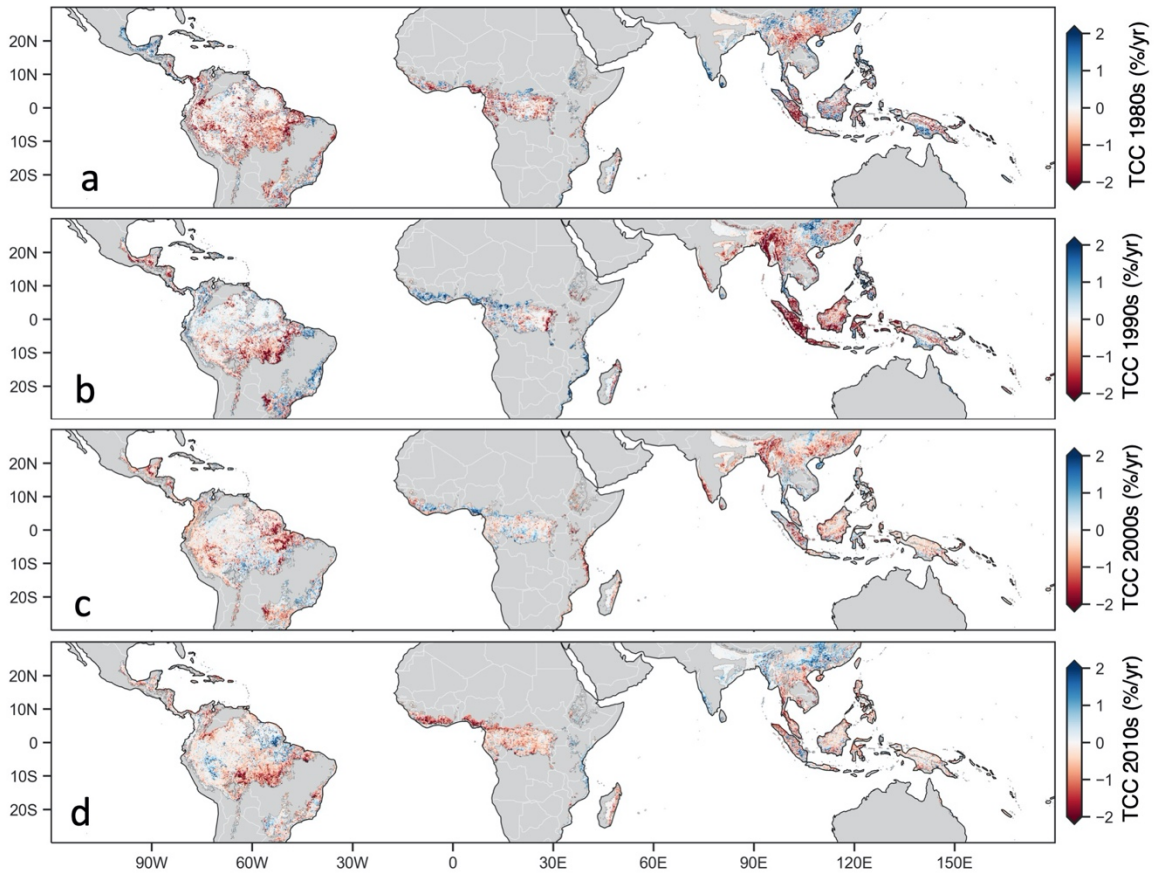


**Figure S2. Decadal tree cover change**. Average annual tree cover change (TCC) across the tropics showing loss and gain of tree cover at 0.1°×0.1° grid cells for (a) 1980s, (b) 1990s, (c) 2000s, and (d) 2010s (2000-2018). Changes of tree cover represent intensification of land use changes from deforestation, degradation, and forest recovery combined by land cover changes associated with environmental factors such as droughts, wildfire, blowdowns, etc.

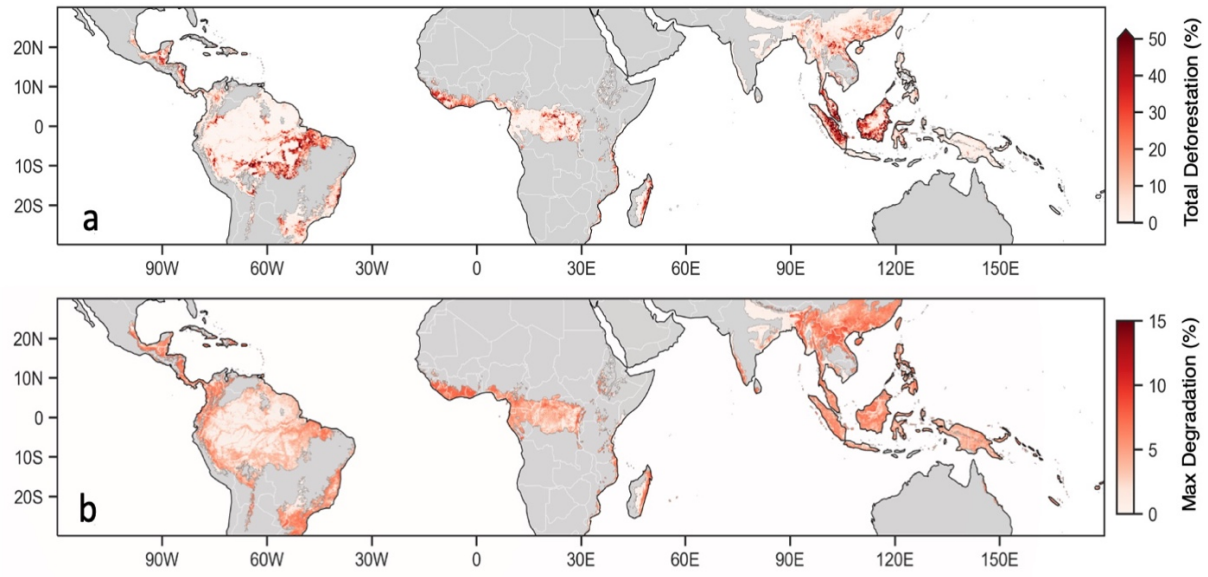


**Figure S3. Areas of forest clearing and degradation:** (a) Total area of deforestation (forest clearing) from 2000-2018 estimated from Landsat time series data at 30 m resolution shown as percent of pixel[2]. (b) Maximum area of pixel (in percent area) of forest degradation from 2000-2018 estimated from a combination of loss of tree cover from forest edges and degradation from logging roads[3].

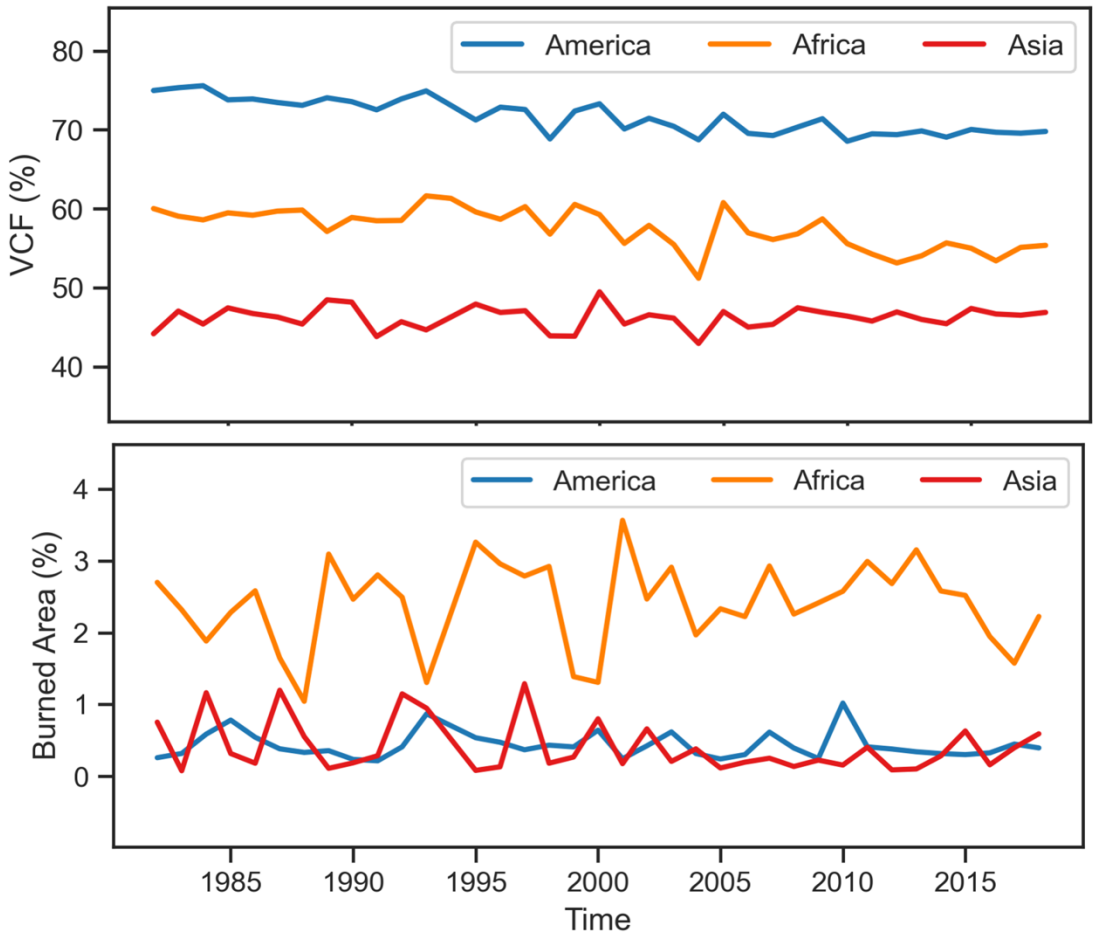


**Figure S4. Areas of forest clearing and degradation:** Top panel shows continental scale changes of tree cover (TC) and fire burned area (BA) showing the extent and trends in net tree loss in America and Africa compared with Asia. Bottom panel compares the extent and the interannual variability of burned areas across the three tropical regions.

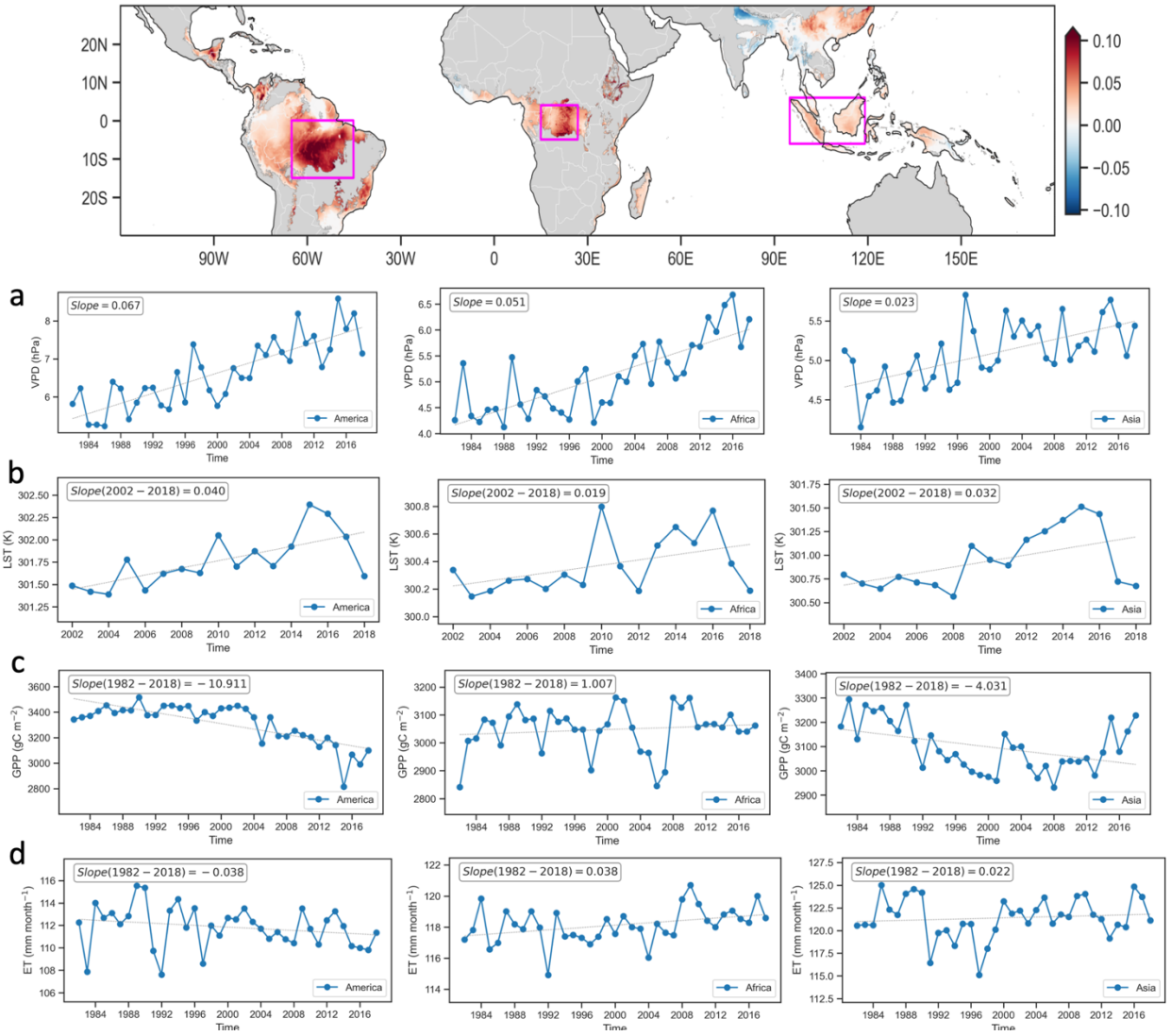


**Figure S5. Long-term temporal variations of stress and response variables.** Aggregated annual patterns in selected boxes of relatively significant change in stress and response variables: top panel is the global trend in VPD and the location of selected continental regions showing (a) VPD annual variations (1982-2018) with steady increase across the three regions, (b) LST annual variations with steady increase from 2000-2016 and decline in years after, (c) GPP annual variations with declining pattern in America, large interannual variability and slight increase in Africa, and a declining trend in Asia that reversed after 2013, and (d) ET variations with declining trend in America, increasing in Africa, and almost no significant trend in Asia.

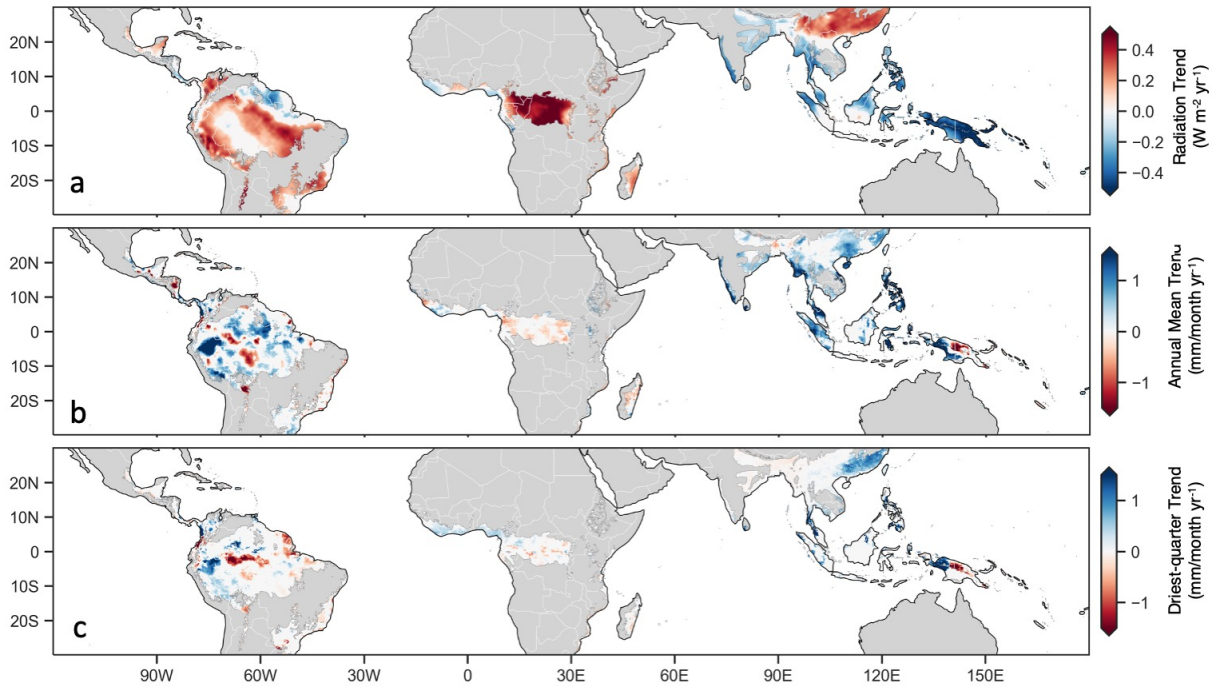


**Figure S6. Long-term precipitation and radiation patterns:** Incoming short-wave radiation is extracted from ERA-5 reanalysis data showing (a) patterns of long-term trend based on monthly data. CHIRPS monthly rainfall data (see Experimental Procedures) are used for developing (b) annual mean rainfall trend from 1982 to 2018, and (c) trend of rainfall driest quarter.

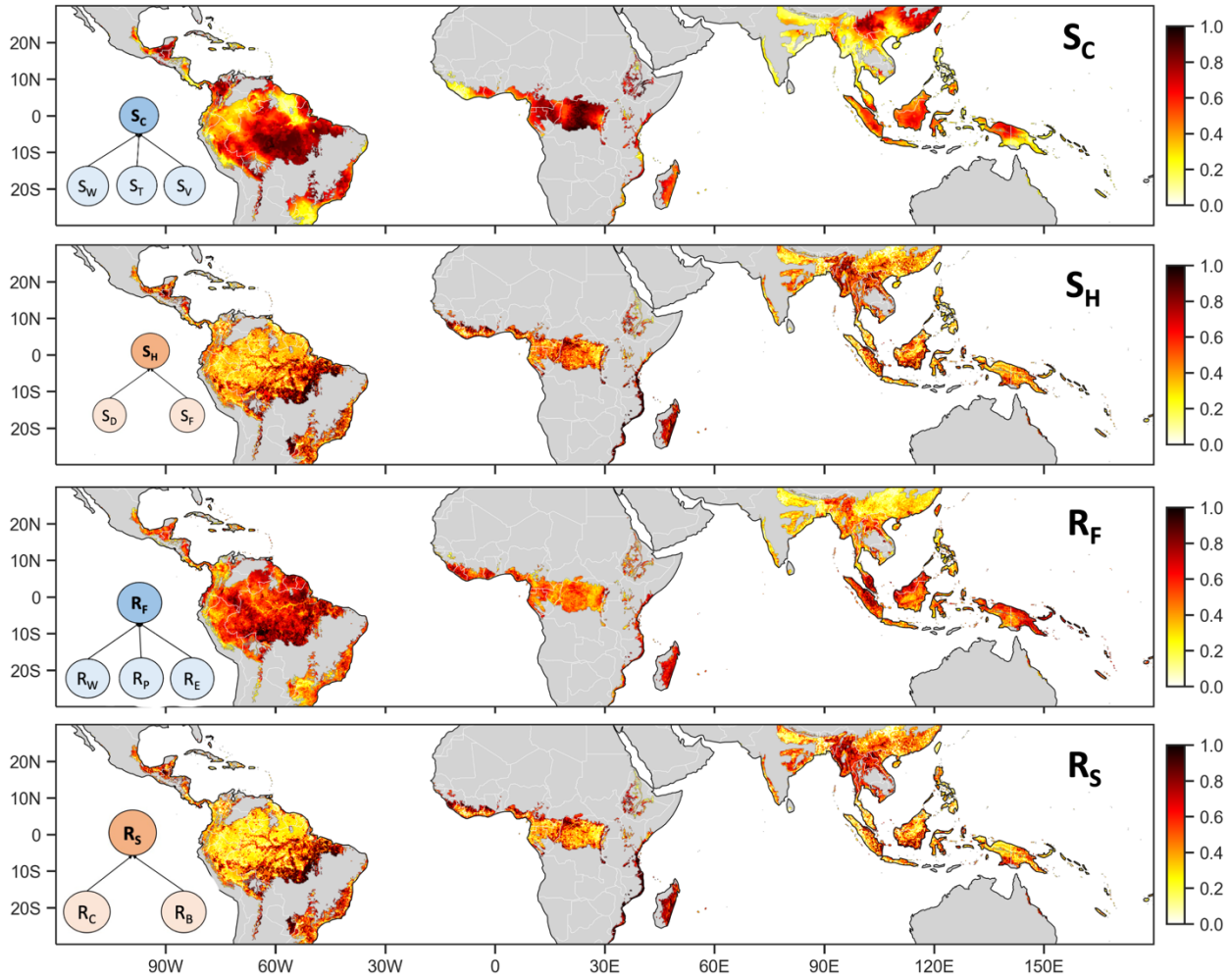


**Figure S7. Spatial patterns of upper level stress and response indices**. The upper-level indices are developed from weighted linear models. (a) climate stress ($S_C$) using normalized individual water, temperature, and VPD variables as $S_C = 0.24 * S_W + 0.23 * S_T + 0.53 * S_V$ (b) human-induced stress ($S_H$) using $S_H = 0.62 * S_D + 0.38 * S_F$ combining tree cover loss and fire, (c) ecosystem function response ($R_F$) from linear combination of normalized LST, GPP, and ET, and (d) ecosystem services response ($R_S$) from linear combination of AGB and biodiversity.

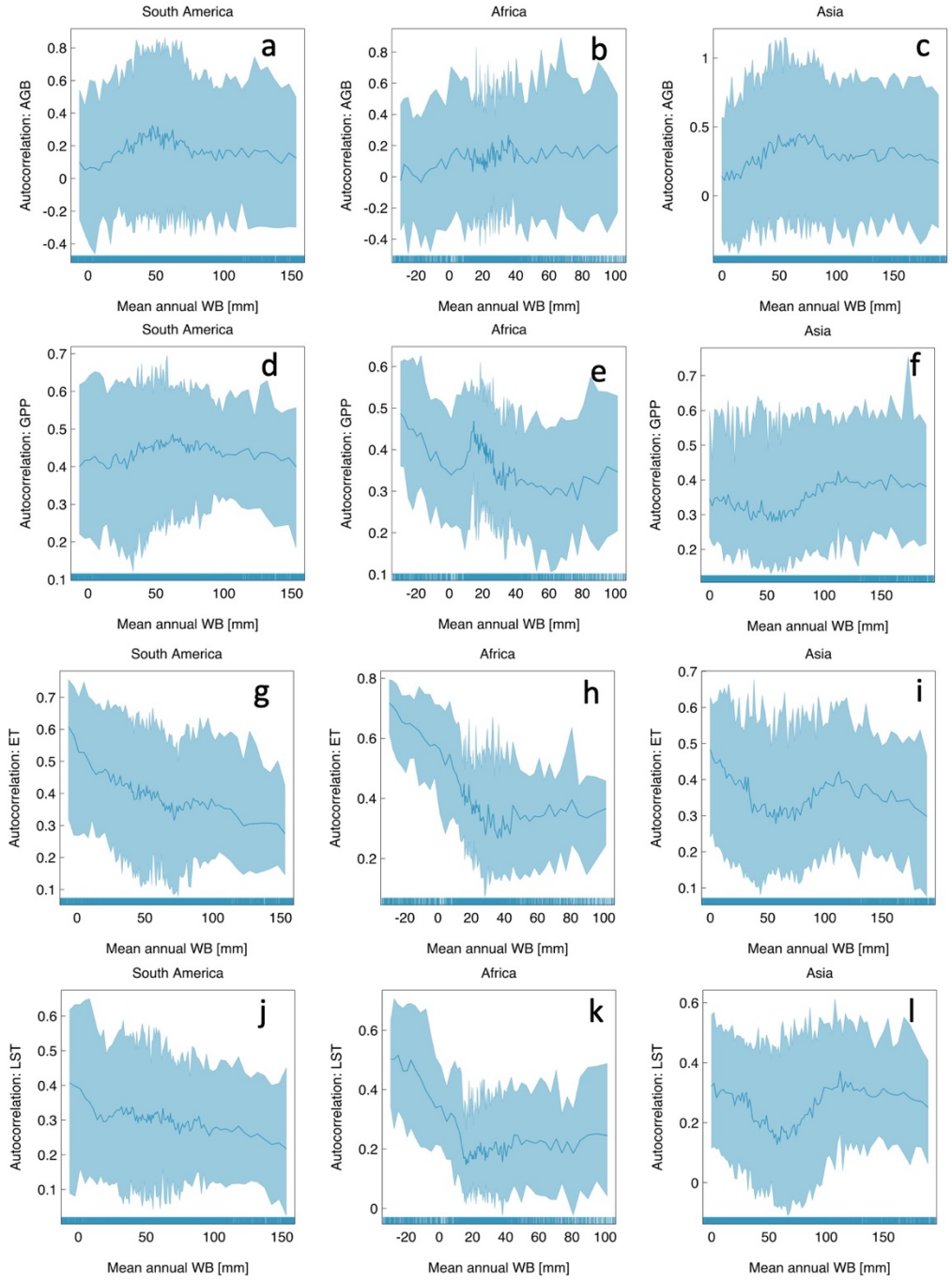


**Figure S8. Variability of autocorrelation of response variables across gradients of water balance (WB).** Distribution of first-order autocorrelation of (a-c) aboveground biomass, (d-f) gross primary productivity, (g-i) evapotranspiration, and (j-l) daytime land surface temperature as a function of the mean water balance in humid tropical forests across (a,d,g,j) South America (b,e,h,k) Africa, and (c,f,i,l) Asia. Lines corresponds to average autocorrelation binned into 1% quantiles along WB gradients, and shaded area represents the 90% range of values within each WB bin. Only the bins between 5$^{th}$ and 95$^{th}$ percentiles of WB are shown.

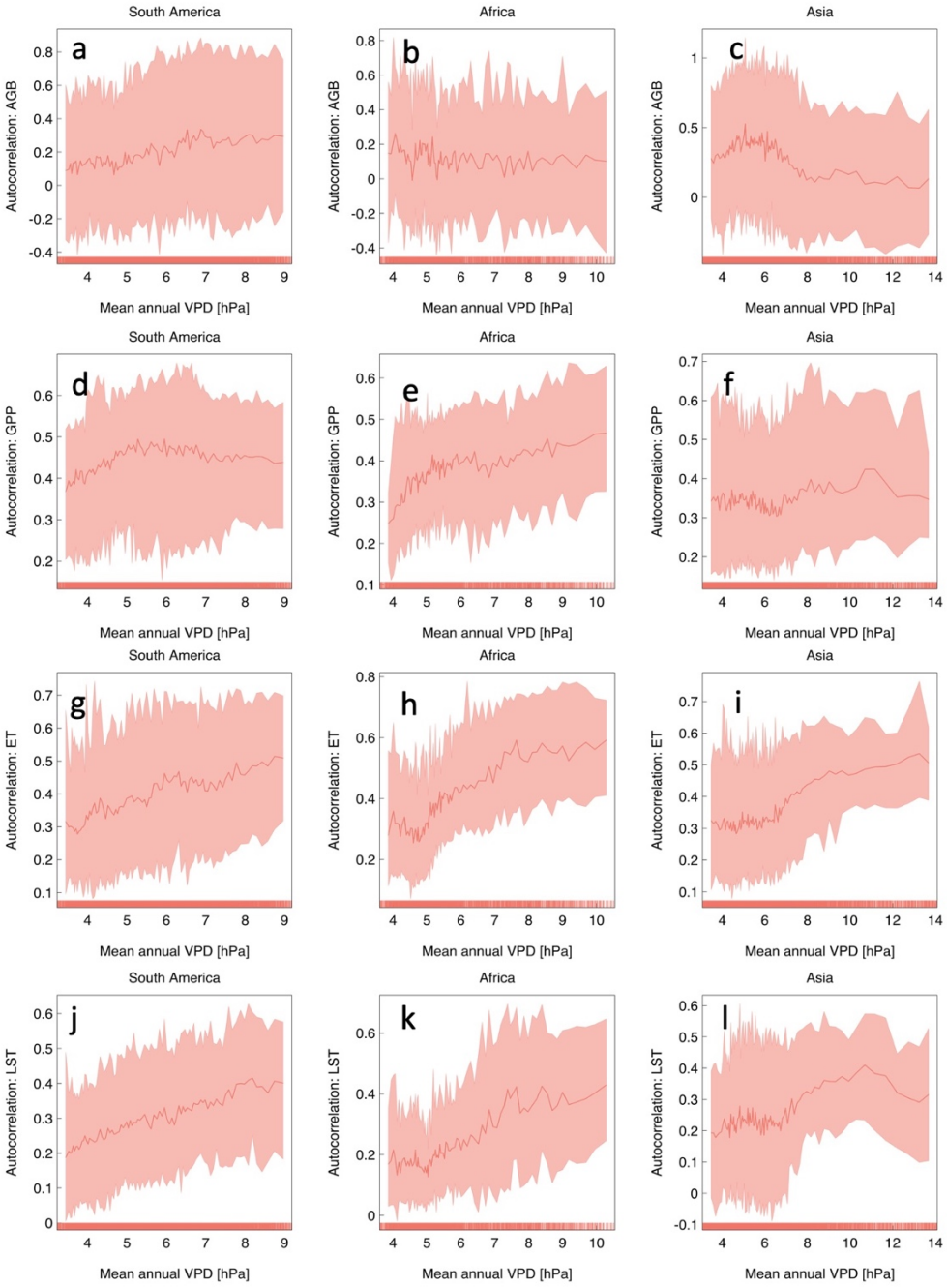


**Figure S9. Variability of autocorrelation of response variables across gradients of vapor pressure deficit (VPD).** Distribution of first-order autocorrelation of (a-c) aboveground biomass, (d-f) gross primary productivity, (g-i) evapotranspiration, and (j-l) daytime land surface temperature as a function of the mean water balance in humid tropical forests across (a,d,g,j) South America (b,e,h,k) Africa, and (c,f,i,l) Asia. Lines corresponds to average autocorrelation binned into 1% quantiles along VPD gradients, and shaded area represents the 90% range of values within each VPD bin. Only the bins between 5$^{th}$ and 95$^{th}$ percentiles of VPD are shown.

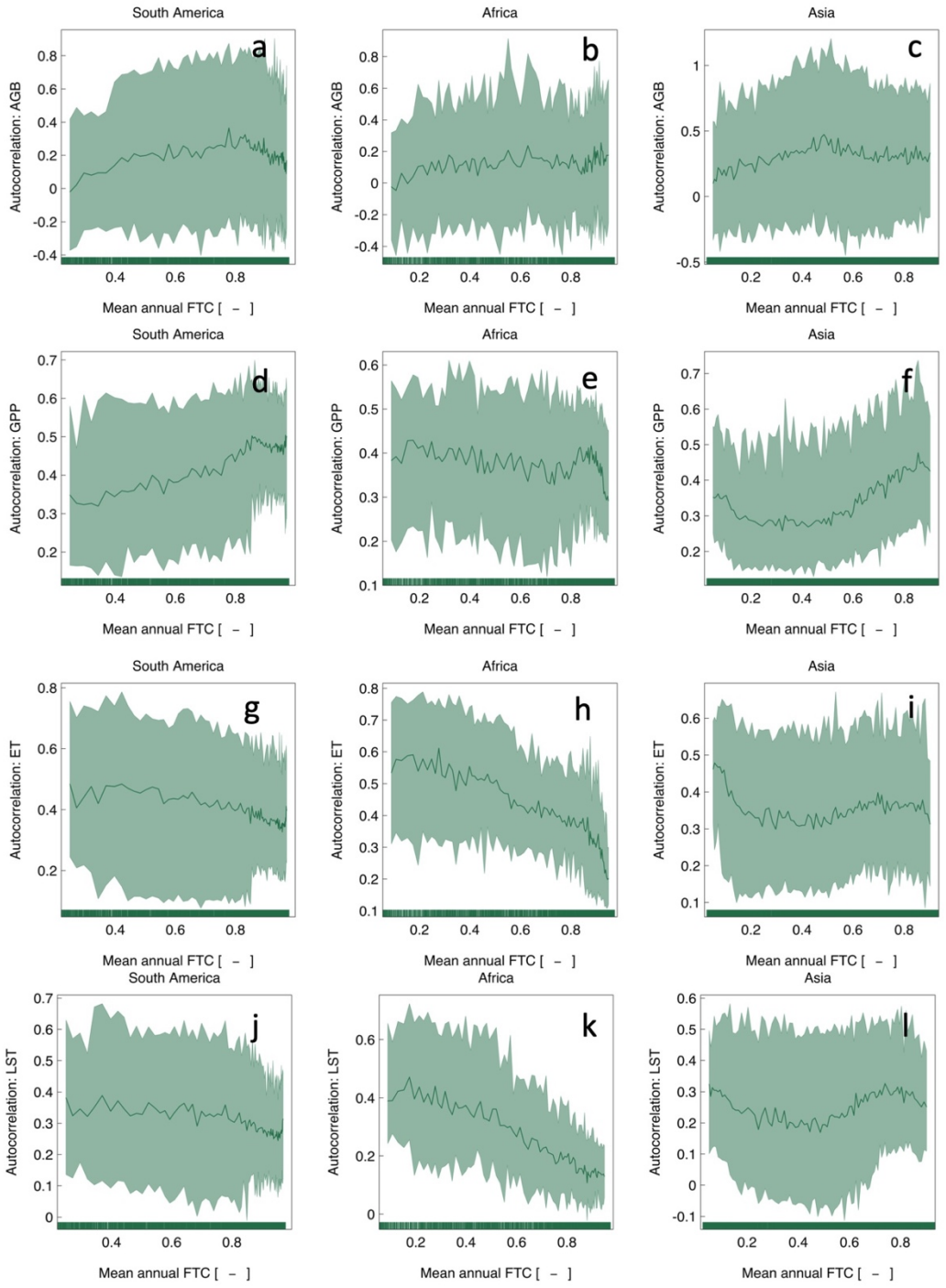


**Figure S10. Variability of autocorrelation of response variables across gradients of fraction of tree cover (FTC).** Distribution of first-order autocorrelation of (a-c) aboveground biomass, (d-f) gross primary productivity, (g-i) evapotranspiration, and (j-l) daytime land surface temperature as a function of the mean water balance in humid tropical forests across (a,d,g,j) South America (b,e,h,k) Africa, and (c,f,i,l) Asia. Lines corresponds to average autocorrelation binned into 1% quantiles along FTC gradients, and shaded area represents the 90% range of values within each FTC bin. Only the bins between 5$^{th}$ and 95$^{th}$ percentiles of FTC are shown.

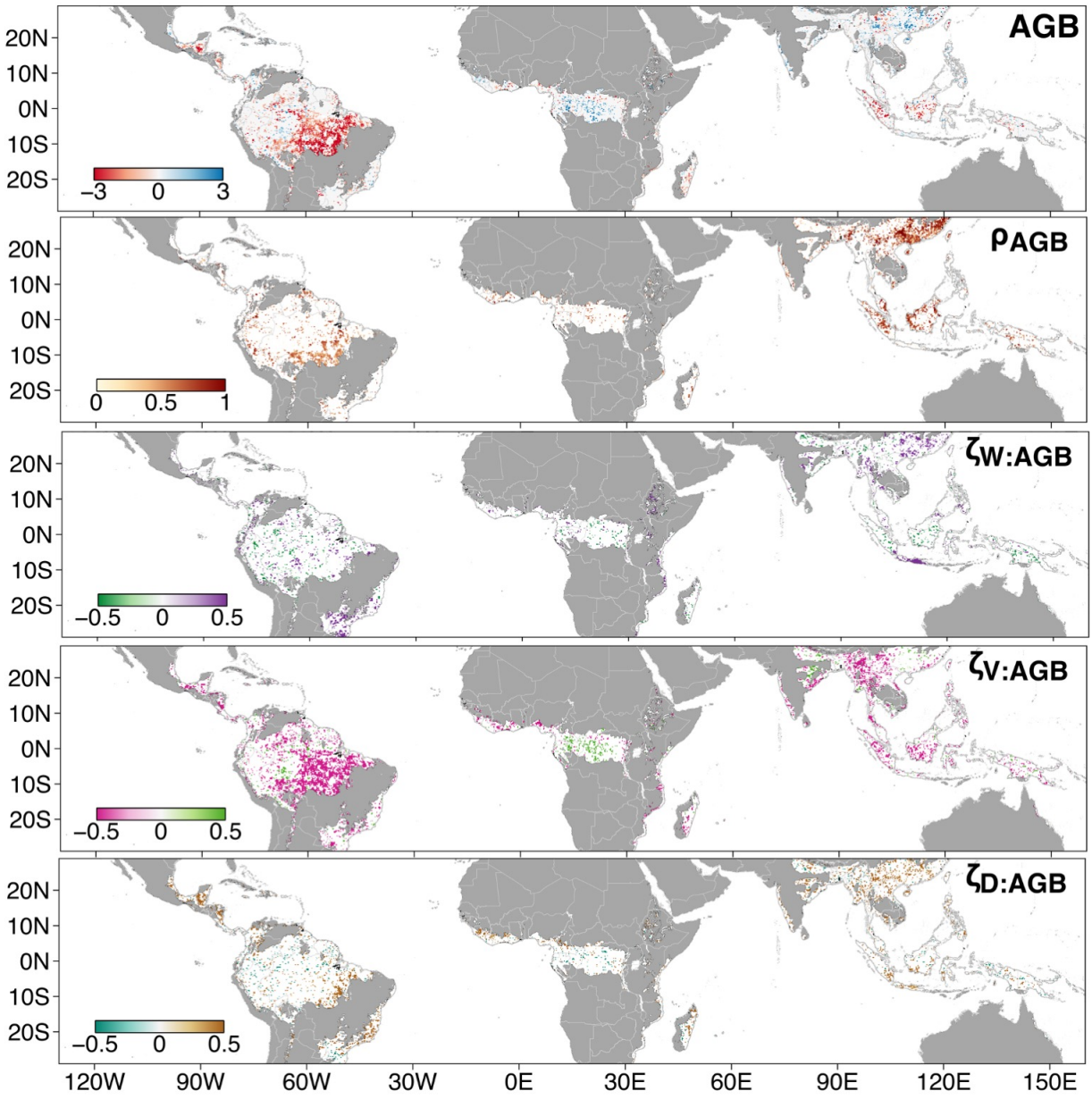


**Figure S11. Spatial patterns of coefficients associated with the vulnerability index for aboveground biomass.** From top to bottom, the maps show the vulnerability index, the autocorrelation term ($\rho_{AGB}$), and the sensitivities to anomalies in water balance ($\zeta_{W:AGB}$), vapor pressure deficit ($\zeta_{V:AGB}$), and tree cover fraction ($\zeta_{D:AGB}$), based on the hybrid first-order autocorrelation model (see Experimental Procedures). Only values different from zero at 95% confidence (based on the robust linear model fitting) are shown.

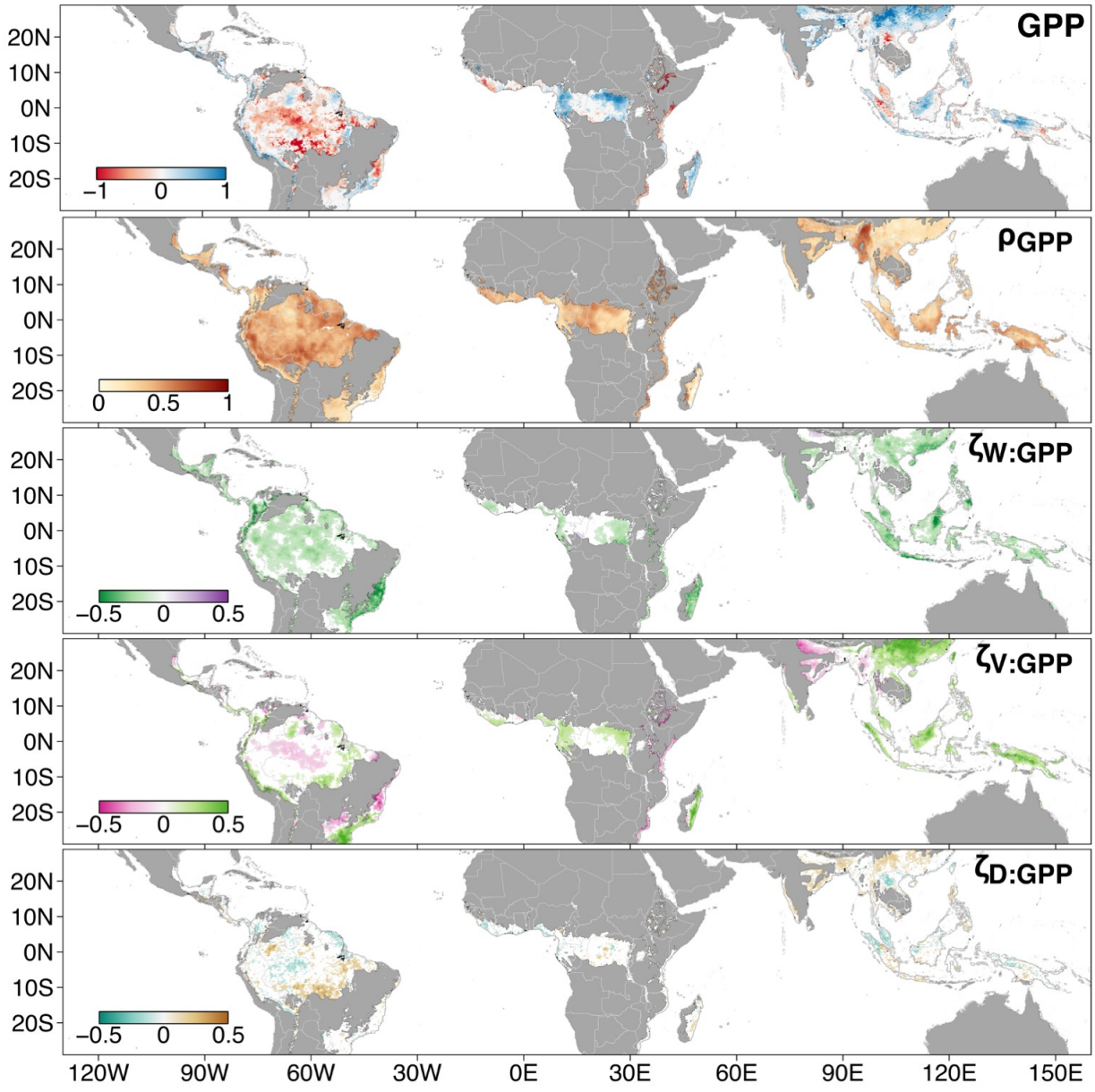


**Figure S12. Spatial patterns of coefficients associated with the vulnerability index for gross primary productivity.** From top to bottom, the maps show the vulnerability index, the autocorrelation term ($\rho_{GPP}$), and the sensitivities to anomalies in water balance ($\zeta_{W:GPP}$), vapor pressure deficit ($\zeta_{V:GPP}$), and tree cover fraction ($\zeta_{D:GPP}$), based on the hybrid first-order autocorrelation model (see Experimental Procedures). Only values different from zero at 95% confidence (based on the robust linear model fitting) are shown.

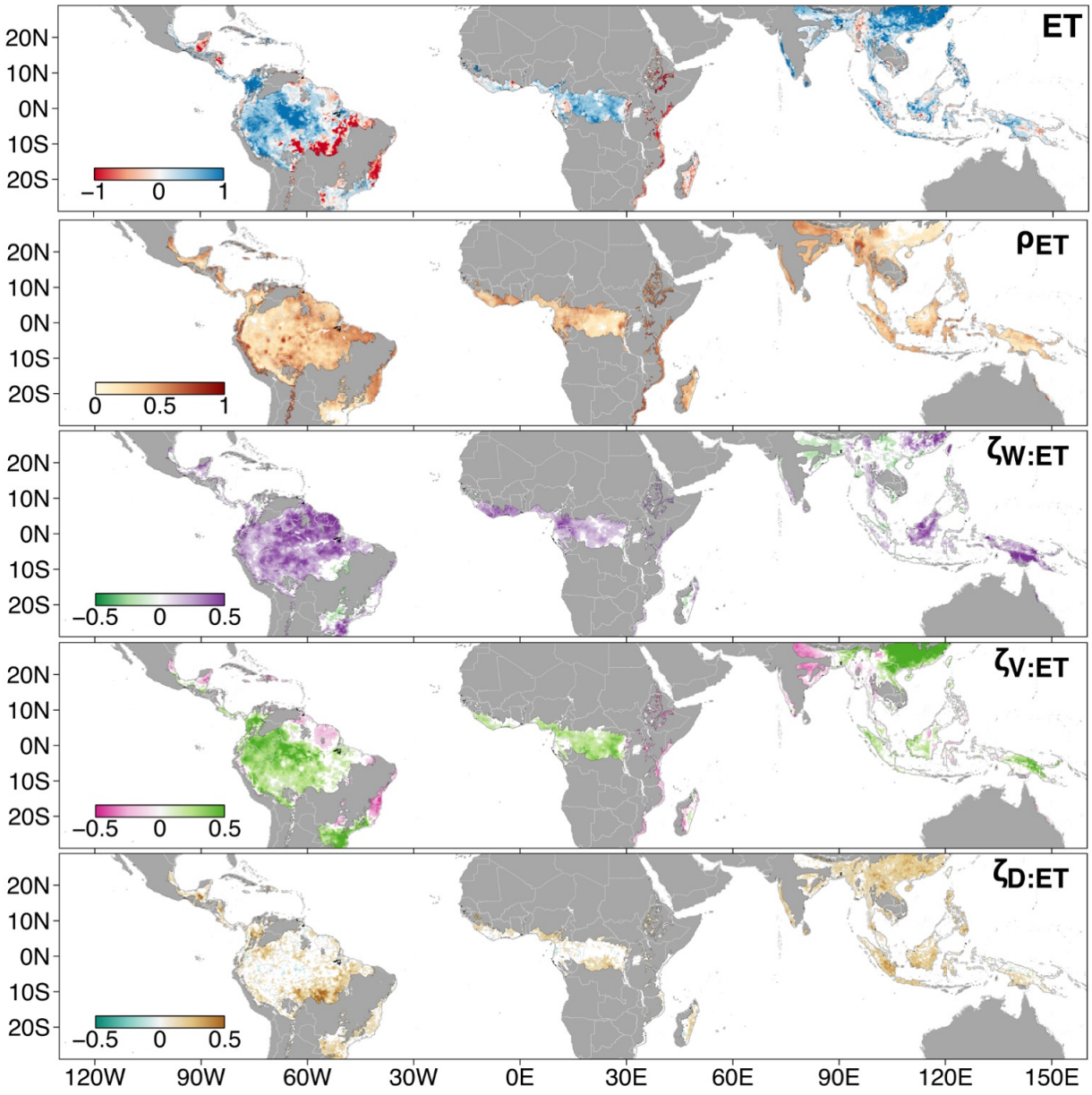


**Figure S13. Spatial patterns of coefficients associated with the vulnerability index for evapotranspiration.** From top to bottom, the maps show the vulnerability index, the autocorrelation term ($\rho_{ET}$), and the sensitivities to anomalies in water balance ($\zeta_{W:ET}$), vapor pressure deficit ($\zeta_{V:ET}$), and tree cover fraction ($\zeta_{D:ET}$), based on the hybrid first-order autocorrelation model (see Experimental Procedures). Only values different from zero at 95% confidence (based on the robust linear model fitting) are shown.

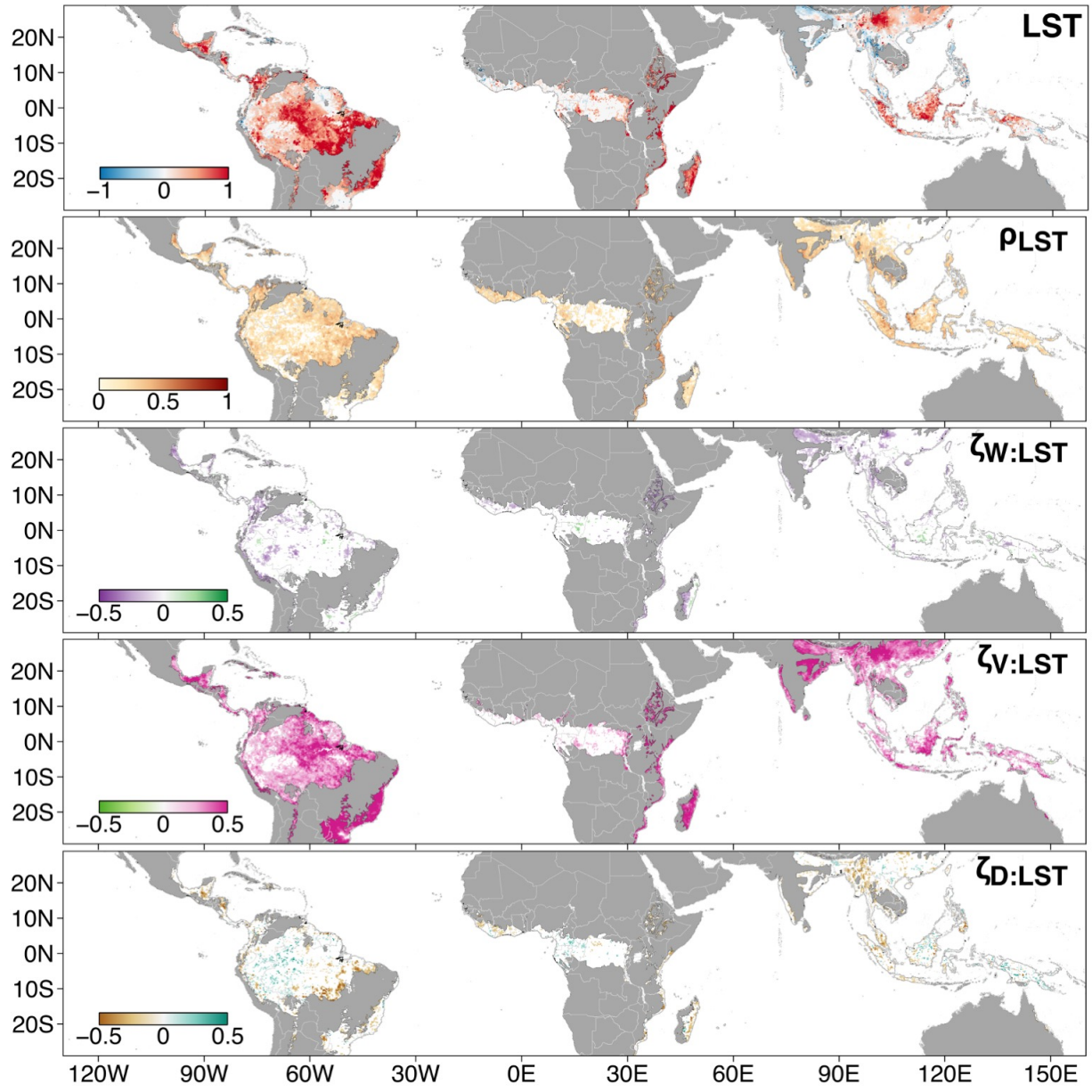


**Figure S14. Spatial patterns of coefficients associated with the vulnerability index for daytime land surface temperature.** From top to bottom, the maps show the vulnerability index, the autocorrelation term ($\rho_{LST}$), and the sensitivities to anomalies in water balance ($\zeta_{W:LST}$), vapor pressure deficit ($\zeta_{V:LST}$), and tree cover fraction ($\zeta_{D:LST}$), based on the hybrid first-order autocorrelation model (see Experimental Procedures). Only values different from zero at 95% confidence (based on the robust linear model fitting) are shown.

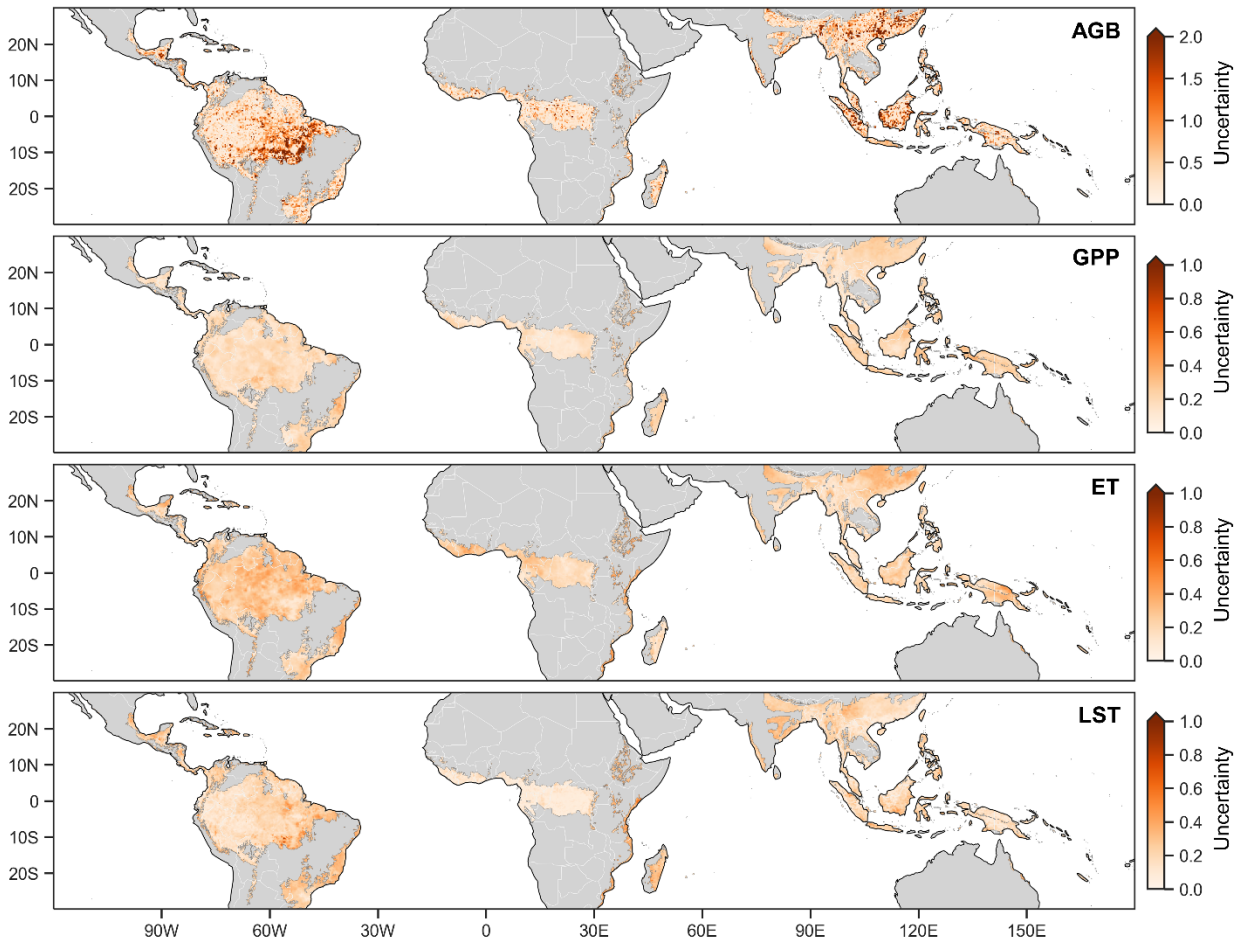


**Figure S15. Spatial patterns of estimated uncertainty associated with the vulnerability indices of response variables (AGB, GPP, ET and LST).** The uncertainty estimation of each variable considered the uncertainty from (1) input long-term trends in water balance, vapor pressure deficit, and tree cover fraction, (2) model uncertainty associated with the estimated coefficients, and (3) the residual errors inherited from the first-order autoregressive model (see Experimental Procedures). Values are shown as 1-sigma errors for all 4 figure panels.

**Table S1.** Continental statistics of biodiversity intactness for areas with different TFVI values. Average biodiversity intactness ($R_B$) for TFVI values that represent vulnerability (TFVI> 0.5 and TFVI < -0.5) and resilience (-0.5 < TFVI < 0.5) are calculated by intersecting spatial products for each response variable with $R_B$ map.

| Tropical Regions | Stats | TFVI condition | GPP | TFVI condition | ET | TFVI condition | LST | TFVI condition | AGB |
|---|---|---|---|---|---|---|---|---|---|
| **Americas** | Area (M km$^2$) | < -0.5 | 1.05 | < -1.0 | 0.49 | < -0.75 | 0.04 | < -1.5 | 1.39 |
| | Biodiversity | | 0.53 | | 0.37 | | 0.40 | | 0.54 |
| | Area (M km$^2$) | [-0.5, 0.5] | 7.80 | [-1.0, 1.0] | 8.05 | [-0.75, 0.75] | 6.91 | [-1.5, 1.5] | 7.53 |
| | Biodiversity | | 0.55 | | 0.55 | | 0.57 | | 0.55 |
| | Area (M km$^2$) | > 0.5 | 0.19 | > 1.0 | 0.53 | > 0.75 | 2.12 | > 1.5 | 0.14 |
| | Biodiversity | | 0.34 | | 0.59 | | 0.45 | | 0.53 |
| **Africa** | Area (M km$^2$) | < -0.5 | 0.19 | < -1.0 | 0.06 | < -0.75 | 0.01 | < -1.5 | 0.10 |
| | Biodiversity | | 0.26 | | 0.23 | | 0.36 | | 0.42 |
| | Area (M km$^2$) | [-0.5, 0.5] | 2.71 | [-1.0, 1.0] | 3.33 | [-0.75, 0.75] | 2.99 | [-1.5, 1.5] | 3.15 |
| | Biodiversity | | 0.48 | | 0.48 | | 0.50 | | 0.48 |
| | Area (M km$^2$) | > 0.5 | 0.51 | > 1.0 | 0.04 | > 0.75 | 0.43 | > 1.5 | 0.18 |
| | Biodiversity | | 0.56 | | 0.41 | | 0.30 | | 0.55 |
| **Asia & Oceania** | Area (M km$^2$) | < -0.5 | 0.13 | < -1.0 | 0.01 | < -0.75 | 0.09 | < -1.5 | 0.26 |
| | Biodiversity | | 0.58 | | 0.44 | | 0.41 | | 0.50 |
| | Area (M km$^2$) | [-0.5, 0.5] | 5.16 | [-1.0, 1.0] | 5.78 | [-0.75, 0.75] | 6.06 | [-1.5, 1.5] | 6.05 |
| | Biodiversity | | 0.47 | | 0.47 | | 0.46 | | 0.46 |
| | Area (M km$^2$) | > 0.5 | 1.14 | > 1.0 | 0.80 | > 0.75 | 0.43 | > 1.5 | 0.27 |
| | Biodiversity | | 0.41 | | 0.43 | | 0.49 | | 0.42 |

**Table S2**. List of science data products used in our study. All satellite data products included uncertainty analysis from a variety of methods. The uncertainty assessment of climate data record required more detailed analysis and was considered outside the scope of our study. The uncertainty estimations for different data products were further described in the Methods section.

| Data sets | Product Name | Satellite Sensor | Spatial resolution | Uncertainty Estimation | Reference |
|---|---|---|---|---|---|
| **Stress Variables** | | | | | |
| **Tree Cover (TC)** | VCF (VCF5KYRv001) | AVHRR | 0.05° | Validation prediction error | [4] |
| | VCF (MOD44B) | MODIS | 250m | Validation prediction error | [5] |
| | Global Forest Change | Landsat | 30m | Validation prediction error | [6] |
| | pantropical degradation project | Landsat | 30m | Bootstrapping Confidence | [7] |
| **Fire Burned Area (BA)** | LTDR burned area | AVHRR | 0.05° | Validation/prediction error | [8] |
| | burned area (MCD64A1 v006) | MODIS | 500m | Validation/prediction error | [9] |
| **Air Temperature (T)** | ERA5 2-m air temperature | Reanalysis | 0.1° | N/A | [10] |
| **Water Balance (WB)** | CHIRPS precipitation | Station TRMM | 0.05° | Validation/prediction error | [11] |
| | GLEAM potential ET | Station Multi-sensor | 0.25° | Validation/prediction error | [12,13] |
| **Vapor Pressure Deficit (VPD)** | ERA5 air temperature | Station Reanalysis | 0.1° | N/A | [10] |
| | ERA5 dewpoint temperature | Station Reanalysis | 0.1° | N/A | [10] |
| **Response Variables** | | | | | |
| **Live Biomass Carbon** | Annual AGC product | GLAS Lidar/Multi-sensor | 0.1° | Error propagation Validation | [14] |
| **Gross Primary Production (GPP)** | Enhanced global GPP | Multi-sensor FluxNet/Model | 1/12° | Validation triple collocation | [15] |
| **Evapotranspiration (ET)** | GLEAM actual evaporation | Station Multi-sensor | 0.25° | Validation triple collocation | [12,13] |
| **Radiative Temperature (LST)** | LST (MOD11A2 v006) | MODIS | 1km | Validation prediction error | [16] |
| **Biodiversity Intactness (BI)** | Biodiversity Intactness Index | Multi-sensor | 1km | Confidence level | [17] |
| | Forest Structural Integrity Index | Multi-sensor | 1km | Confidence level | [18] |

## References


1. Olson, D.M., Dinerstein, E., Wikramanayake, E.D., Burgess, N.D., Powell, G.V.N., Underwood, E.C., D'Amico, J.A., Itoua, I., Strand, H.E., Morrison, J.C., et al. (2001). Terrestrial ecoregions of the world: A new map of life on Earth. Bioscience *51*, 933–938.

2. Hansen, M.C., Potapov, P. V., Moore, R., Hancher, M., Turubanova, S.A., Tyukavina, A., Thau, D., Stehman, S. V., Goetz, S.J., Loveland, T.R., et al. (2013). High-resolution global maps of 21st-century forest cover change. Science (80-. ). *342*, 850–853.

3. Maxwell, S.L., Evans, T., Watson, J.E.M., Morel, A., Grantham, H., Duncan, A., Harris, N., Potapov, P., Runting, R.K., Venter, O., et al. (2019). Degradation and forgone removals increase the carbon impact of intact forest loss by 626%. Sci. Adv. *5*, eaax2546–eaax2546.

4. Song, X.P., Hansen, M.C., Stehman, S. V., Potapov, P. V., Tyukavina, A., Vermote, E.F., and Townshend, J.R. (2018). Global land change from 1982 to 2016. Nature *560*, 639–643.

5. Dimiceli C., Carroll, M., Sohlberg R. Kim, D.H., Kelly, M., and Townshend, J.R.G. (2015). {MOD44B} {MODIS}/{T}erra vegetation continuous fields yearly {L3} Global 250m {SIN} Grid {V006}.

6. Hansen, M.C., Potapov, P. V., Moore, R., Hancher, M., Turubanova, S.A., Tyukavina, A., Thau, D., Stehman, S. V., Goetz, S.J., Loveland, T.R., et al. (2013). High-Resolution Global Maps of 21st-Century Forest Cover Change. Science (80-. ). *342*, 850–853.

7. Maxwell, S.L., Evans, T., Watson, J.E.M., Morel, A., Grantham, H., Duncan, A., Harris, N., Potapov, P., Runting, R.K., Venter, O., et al. (2019). Degradation and forgone removals increase the carbon impact of intact forest loss by 626%. Sci. Adv. *5*.

8. Otón, G., Ramo, R., Lizundia-Loiola, J., and Chuvieco, E. (2019). Global Detection of Long-Term (1982–2017) Burned Area with AVHRR-LTDR Data. Remote Sens. *11*, 2079.

9. Giglio, L., Boschetti, L., Roy, D.P., Humber, M.L., and Justice, C.O. (2018). The Collection 6 MODIS burned area mapping algorithm and product. Remote Sens. Environ. *217*, 72–85.

10. Hersbach, H., Bell, B., Berrisford, P., Hirahara, S., Horányi, A., Muñoz-Sabater, J., Nicolas, J., Peubey, C., Radu, R., Schepers, D., et al. (2020). The ERA5 global reanalysis. Q. J. R. Meteorol. Soc. *146*, 1999–2049.

11. Funk, C., Peterson, P., Landsfeld, M., Pedreros, D., Verdin, J., Shukla, S., Husak, G., Rowland, J., Harrison, L., Hoell, A., et al. (2015). The climate hazards infrared precipitation with stations - A new environmental record for monitoring extremes. Sci. Data *2*.

12. Miralles, D.G., Holmes, T.R.H., De Jeu, R.A.M., Gash, J.H., Meesters, A.G.C.A., and

Dolman, A.J. (2011). Global land-surface evaporation estimated from satellite-based observations. Hydrol. Earth Syst. Sci. *15*, 453–469.

13. Martens, B., Miralles, D.G., Lievens, H., Van Der Schalie, R., De Jeu, R.A.M., Fernández-Prieto, D., Beck, H.E., Dorigo, W.A., and Verhoest, N.E.C. (2017). GLEAM v3: Satellite-based land evaporation and root-zone soil moisture. Geosci. Model Dev. *10*, 1903–1925.

14. Xu, L., Saatchi, S., Yang, Y., et, al (2020). Live Vegetation Biomass Controls Terrestrial Carbon Sources and Sinks. Rev.

15. Madani, N., et al. (2020). Recent Amplified Global Gross Primary Productivity Due to Temperature Increase is 1 offset by Reduced Productivity Due to Water Constraints. Agu Adv.

16. Wan, Z., Hook, S., and Hulley, G. (2015). {MOD11C3} {MODIS}/{T}erra land surface temperature/emissivity {L3} Global 0.05Deg {CMG} Grid {V006}.

17. Newbold, T., Hudson, L.N., Arnell, A.P., Contu, S., De Palma, A., Ferrier, S., Hill, S.L.L., Hoskins, A.J., Lysenko, I., Phillips, H.R.P., et al. (2016). Has land use pushed terrestrial biodiversity beyond the planetary boundary? A global assessment. Science (80-. ). *353*, 291–288.

18. Hansen, A., Barnett, K., Jantz, P., Phillips, L., Goetz, S.J., Hansen, M., Venter, O., Watson, J.E.M., Burns, P., Atkinson, S., et al. (2019). Global humid tropics forest structural condition and forest structural integrity maps. Sci. data *6*, 232.